Article

Clostridioides difficile ferrosome organelles combat nutritional immunity

Check for updates

Hualiang Pi[1,2,11,12], Rong Sun[3,4,5,6,12], James R. McBride[7], Angela R. S. Kruse[8,9], Katherine N. Gibson-Corley[2], Evan S. Krystofiak[3], Maribeth R. Nicholson[10], Jeffrey M. Spraggins[3,8,9], Qiangjun Zhou[3,4,5,6]✉ & Eric P. Skaar[1,2]✉

Iron is indispensable for almost all forms of life but toxic at elevated levels[1–4]. To survive within their hosts, bacterial pathogens have evolved iron uptake, storage and detoxification strategies to maintain iron homeostasis[1,5,6]. Recent studies showed that three Gram-negative environmental anaerobes produce iron-containing ferrosome granules[7,8]. However, it remains unclear whether ferrosomes are generated exclusively by Gram-negative bacteria. The Gram-positive bacterium *Clostridioides difficile* is the leading cause of nosocomial and antibiotic-associated infections in the USA[9]. Here we report that *C. difficile* undergoes an intracellular iron biomineralization process and stores iron in membrane-bound ferrosome organelles containing non-crystalline iron phosphate biominerals. We found that a membrane protein (FezA) and a P_{1B6}-ATPase transporter (FezB), repressed by both iron and the ferric uptake regulator Fur, are required for ferrosome formation and play an important role in iron homeostasis during transition from iron deficiency to excess. Additionally, ferrosomes are often localized adjacent to cellular membranes as shown by cryo-electron tomography. Furthermore, using two mouse models of *C. difficile* infection, we demonstrated that the ferrosome system is activated in the inflamed gut to combat calprotectin-mediated iron sequestration and is important for bacterial colonization and survival during *C. difficile* infection.

Clostridioides difficile, a Gram-positive, spore-forming anaerobe, is an urgent threat to global public health and causes approximately half a million infections and more than 29,000 deaths annually[9]. Current treatments are limited to last resort antibiotics, such as fidaxomicin or vancomycin, and in more serious cases faecal microbiota transplantation or surgery[10,11]. Even with treatment, the rate of recurrence of *C. difficile* infection (CDI) is 20–25% and one in nine patients over 65 will die within 30 days after diagnosis[12]. These facts highlight the importance of identifying alternative strategies for the treatment of CDI.

The pathogenesis of *C. difficile* is dependent on its ability to acquire nutrient metals for colonization and proliferation[13–15]. To inhibit microbial replication, vertebrate hosts have evolved defence strategies to sequester metals from invading pathogens, known as nutritional immunity. Nutritional immunity is a potent defence against CDI[13–15] in which nutrient metals are withheld by host proteins such as calprotectin (CP), lipocalin-2 (LCN-2) and lactoferrin[16,17]. CP is a heterodimer of two S100 calcium binding proteins, S100A8 and S100A9. CP makes up about 50% of the protein composition within the neutrophil cytoplasm, and restricts multiple metals including zinc, manganese and iron[14,18,19]. LCN-2 (also known as neutrophil-associated gelatinase lipocalin, NAGL) sequesters

siderophores, which are small iron-chelating molecules[20]. Lactoferrin, a cationic glycosylated transferrin family protein, primarily sequesters iron at mucosal surfaces[21]. These proteins possess broad antimicrobial activities against bacterial pathogens, exhibit potent immunomodulatory effects[19,21–25] and serve as common clinical inflammatory biomarkers with their abundance positively correlating with CDI severity[26–29]. However, it is unclear how *C. difficile* adapts to iron limitation mediated by these proteins and how this pathogen resists nutritional immunity during infection. Here, we discovered that *C. difficile* produces iron phosphate-containing ferrosome organelles to prevent iron intoxication during transient iron overload in vitro. Furthermore, we demonstrated that the ferrosome system is activated during CDI and is important for subverting nutritional immunity and overcoming iron stress in the mammalian gut. These results highlight the potential of targeting ferrosome formation as a new antimicrobial strategy against this important pathogen.

An iron storage system in *C. difficile*

The iron homeostasis systems of *C. difficile* are largely uncharacterized. Thus, we set out to identify these systems and examine

[1]Vanderbilt Institute for Infection, Immunology, and Inflammation, Vanderbilt University, Nashville, TN, USA. [2]Department of Pathology, Microbiology, & Immunology, Vanderbilt University Medical Center, Nashville, TN, USA. [3]Department of Cell and Developmental Biology, Vanderbilt University, Nashville, TN, USA. [4]Vanderbilt Brain Institute, Vanderbilt University School of Medicine, Nashville, TN, USA. [5]Center for Structural Biology, Vanderbilt University School of Medicine, Nashville, TN, USA. [6]Vanderbilt Kennedy Center, Vanderbilt University Medical Center, Nashville, TN, USA. [7]Vanderbilt Institute of Nanoscale Science and Engineering, Vanderbilt University, Nashville, TN, USA. [8]Mass Spectrometry Research Center, Vanderbilt University Medical Center, Nashville, TN, USA. [9]Department of Biochemistry, Vanderbilt University Medical Center, Nashville, TN, USA. [10]Department of Pediatrics, Vanderbilt University Medical Center, Nashville, TN, USA. [11]Present address: Department of Microbial Pathogenesis and Microbial Sciences Institute, Yale University School of Medicine, New Haven, CT, USA. [12]These authors contributed equally: Hualiang Pi, Rong Sun. ✉e-mail: qiangjun.zhou@Vanderbilt.Edu; eric.skaar@vumc.org
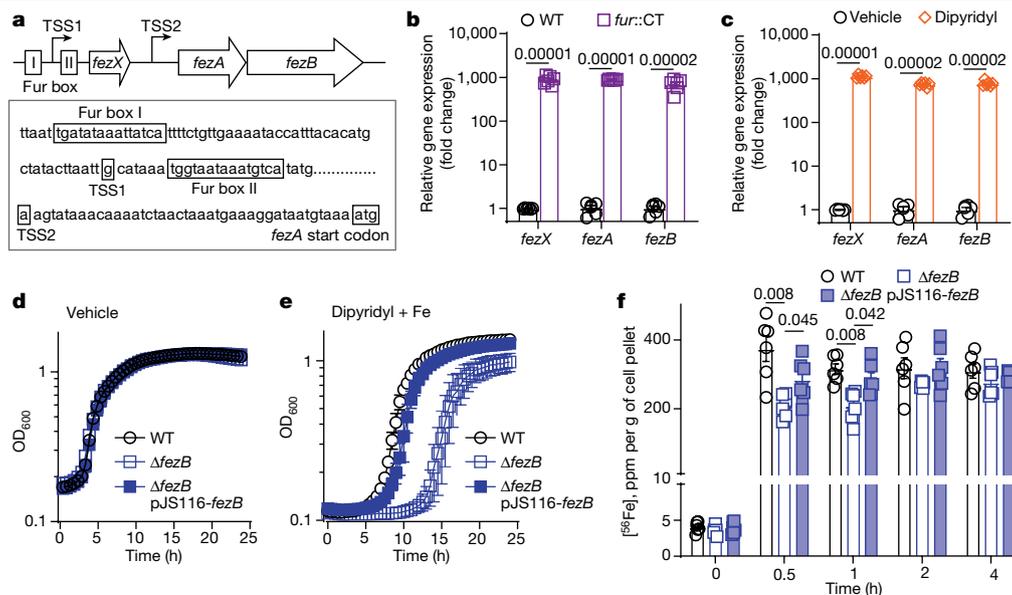
Fig. 1 | FezB, regulated by Fur and iron, plays a critical role in maintaining iron homeostasis during the transition from iron deficiency to excess.
a, The 5′ untranslated region of *fezAB* contains two putative Fur boxes and a small transcript (*fezX*). The two transcription start sites (TSS1 and TSS2) were mapped by 5′ rapid amplification of complementary DNA ends (5′ RACE). **b**,**c**, Expression of *fezXAB* was quantified by qPCR in WT and *fur*::CT (**b**) or in WT following vehicle or 100 µM dipyridyl treatment (**c**). **d**,**e**, The growth kinetics of *C. difficile* WT, Δ*fezB* and the complemented strain Δ*fezB* pJS116-*fezB* grown under vehicle (BHIS) (**d**) or during the transition from iron deficiency (100 µM dipyridyl) to excess following addition of 1 mM FeSO₄ (**e**). **f**, Intracellular iron was monitored using ICP-MS for 4 h after 1 mM FeSO₄ was added to cultures of *C. difficile* WT, Δ*fezB* and Δ*fezB* pJS116-*fezB* cells grown in BHIS amended with 100 µM dipyridyl. The data are expressed as ppm per gram of cell pellet. Experiments were conducted three (**b**–**e**) or two (**f**) times independently with similar results. Data are presented as mean ± s.d., *n* = 6 (**b**,**c**); mean ± s.d., *n* = 6 (**d**,**e**); mean ± s.e.m., *n* = 6 (**f**). Significant differences were determined by two-tailed *t*-tests and the *P* values are denoted in the graphs. OD₆₀₀, optical density at 600 nm.

their physiological roles. Two genes that lack annotated functions, *CD196_0533* and *CD196_0534*, were among the most upregulated genes on iron deprivation[30]. CD196_0533 shares over 30% sequence identity with a predicted P₁ᵦ₆-ATPase transporter FezB that is required for ferrosome formation in three Gram-negative environmental anaerobes[8]. Thus, we have named CD196_0533 FezB and the predicted membrane protein (CD196_0534) FezA. Two putative Fur boxes, two transcription start sites and an 87 base pair (bp) gene (which we refer to here as *fezX*) were identified in the promoter region of *fezA* and *fezB* (Fig. 1a). The regulatory role of the ferric uptake regulator (Fur) and iron in transcription of *fezXAB* was further validated by quantitative polymerase chain reaction (qPCR). The transcription of all three genes is derepressed in a mutant with disrupted activity of Fur (*fur*::CT), compared with wild type (WT) (Fig. 1b), and strongly induced upon iron limitation mediated by the iron chelator dipyridyl (Fig. 1c). To further elucidate the physiological function of FezB, we constructed a clean deletion mutant of *fezB* (Δ*fezB*) using a CRISPR–Cas9 editing system[31] and characterized this mutant using a growth assay under various stress conditions. In *Shewanella putrefaciens* ferrosomes support anaerobic growth in low iron conditions[8]. No growth defects were observed between Δ*fezB* and WT *C. difficile* grown under iron excess or limitation whereas a moderate phenotype was noted in the presence of both dipyridyl and H₂O₂ (Extended Data Fig. 1), indicating that FezB does not play a role in iron import or export but is important in protection against oxidative stress. Interestingly, Δ*fezB* exhibited an extended lag phase compared with WT when excess FeSO₄ (1 mM) was added to iron-starved cells and this phenotype was complemented by expression of FezB in trans (Δ*fezB* pJS116-*fezB*) (Fig. 1d,e), demonstrating that FezB is important for maintaining iron homeostasis during the transition from iron deficiency to excess. To further investigate the function of FezB, we monitored intracellular metal ion levels over a time-course using inductively coupled plasma mass spectrometry (ICP-MS). No significant differences in iron levels were observed among the strains tested under iron-deficient

conditions (brain–heart-infusion broth (BHIS) supplemented with yeast extract + dipyridyl); however, Δ*fezB* exhibited a significantly reduced level of intracellular iron compared with WT within the first hour during the transition from iron deficiency to excess (Fig. 1f). Other metals were not affected by loss of FezB (Extended Data Fig. 2). Together, these data suggest that FezB may not function in iron import or export but may serve as part of an iron storage mechanism. We suggest that the Fez system is induced upon iron limitation in anticipation of iron overload following transition of iron-restricted cells, which express high-affinity import systems, to an iron replete environment. Expression of the Fez system equips *C. difficile* with a capacity for iron storage and thereby defends against transient iron overload while simultaneously storing iron for later use under iron-limiting conditions.

FezB is required for granule formation

Three Gram-negative environmental anaerobes were found to produce electron-dense iron granules (named ferrosomes) in a FezB-dependent manner[7,8]. We therefore proposed that FezB is required for ferrosome formation in *C. difficile*. To test this, scanning transmission electron microscopy (STEM) was used to visualize electron-dense granules using the high-angle annular dark-field (HAADF) detector. Following addition of iron to iron-starved cells, faceted electron-dense granules were detected in *C. difficile* WT cells (Fig. 2a). These granules were not present in Δ*fezB* and only disordered iron precipitates could be visualized in this strain (Fig. 2b). Providing *fezB* in trans restored granule formation (Fig. 2c). Because *fezB* is highly upregulated in a *fur*::CT mutant (Fig. 1b), we proposed that these granules are constitutively produced in *fur*::CT. Indeed, many clusters of granules were observed in *fur*::CT (Fig. 2d), and deletion of *fezB* in the *fur*::CT background abolished granule formation (Fig. 2e). *C. difficile* WT and the complemented strain produced about 10 granules per cell, *fur*::CT produced more than 100 granules per cell, whereas neither Δ*fezB* nor *fur*::CT Δ*fezB* generated detectable granules
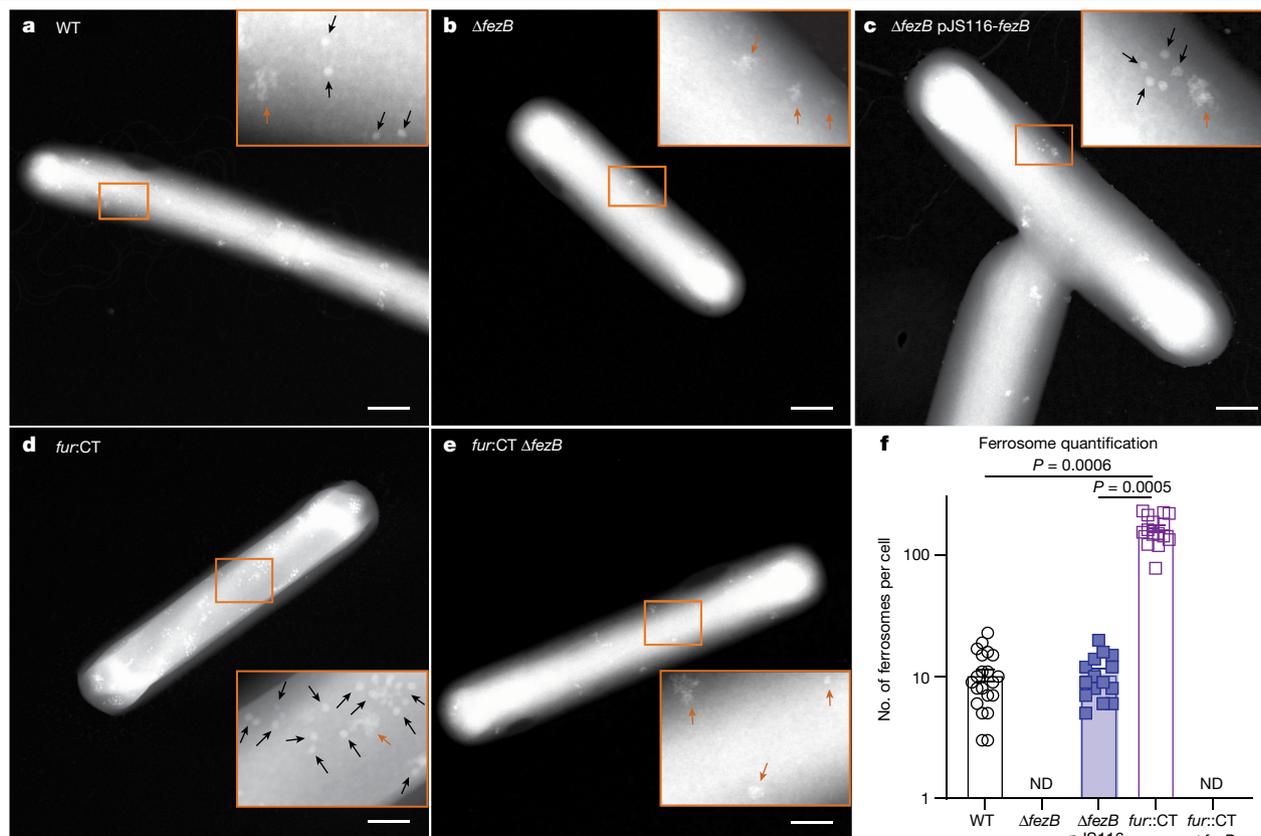
Fig. 2 | FezB is required for intracellular biomineralization in *C. difficile*.
a–**e**, Electron-dense granules were visualized using the HAADF detector of the scanning transmission electron microscope. Representative images shown are WT (**a**), Δ*fezB* (**b**), Δ*fezB* pJS116-*fezB* (**c**), *fur*::CT (**d**) and *fur*::CT Δ*fezB* (**e**). Insets, the faceted granules are denoted by black arrows whereas disordered iron precipitates are indicated by orange arrows. Scale bars, 500 nm. **f**, Numbers of ferrosomes were quantified in individual cells of each strain and data are presented as mean ± s.e.m. (*n* = 20). Statistical analyses were done using one-way analysis of variance (ANOVA) and the *P* values are denoted in the graph. ND, not detectable.

(Fig. 2f). These data demonstrate that FezB is required for formation of electron-dense granules in *C. difficile*.

Intracellular iron phosphate ferrosomes

To determine the elemental composition of the electron-dense granules, energy dispersive X-ray spectroscopy (EDS) was used. Because these granules are constitutively produced in *fur*::CT cells (Fig. 2d), this mutant was subjected to EDS analysis, which showed that elemental iron (Fe) signal colocalizes with the electron-dense granules (Fig. 3a–c and Extended Data Fig. 3a). Given the ubiquity of oxygen (O)- and phosphorus (P)-containing organic molecules in cells, the entire cellular space showed faint O and P signals; however, strong O and P foci were visible within *C. difficile* and colocalize with Fe signal and electron-dense granules (Fig. 3a–e). By contrast, a moderate calcium (Ca) signal was observed throughout the cell, but no Ca foci were present (Fig. 3f and Extended Data Fig. 3a). These data indicate that only Fe, O and P specifically accumulate in these ferrosomes.

To examine whether ferrosomes are localized on the *C. difficile* cell surface, membrane or in the cytoplasm, electron tomography was used, enabling three-dimensional (3D) reconstruction of subcellular structures. The electron tomograph of an intact *fur*::CT cell showed that the majority of the ferrosomes are localized in the cytosol with some ferrosomes being detectable underneath the membrane and a few located outside of the cell, possibly due to cell lysis during sample preparation (Fig. 3g–i and Supplementary Video 1). To further define the localization and elemental composition of these ferrosomes, freeze-substitution was carried out using *fur*::CT cells. Cells were stained with uranyl acetate

to stabilize the membrane and cell wall, and ultrathin sections (100 nm) were processed and subjected to STEM–EDS imaging. STEM imaging confirmed that ferrosomes are localized in the cytoplasm and EDS analysis showed that ferrosomes contain only Fe, O and P (Fig. 3j–o and Extended Data Fig. 3b). Furthermore, the ferrosome system is present in many *C. difficile* clinical isolates representing various ribotypes, and electron-dense granules with similar chemical composition of Fe, O and P were detectable in a representative clinical isolate (Supplementary Table 1 and Extended Data Fig. 4).

Next, ferrosomes were isolated from cell lysates of *C. difficile fur*::CT using a sucrose cushion approach[8]. Selected area electron diffraction was carried out; however, no crystalline lattice structures were visible in these ferrosomes (Extended Data Fig. 5a,b). The electron-dense regions of the ferrosomes are approximately 18 nm in Ferret diameter on the basis of micrographs obtained via transmission electron microscopy (TEM). EDS analysis further confirmed that isolated ferrosomes are iron phosphate granules with the ratio of Fe to P being around 1:1 (Extended Data Fig. 5c–j). Taken together, these microscopic analyses demonstrate that *C. difficile* produces intracellular ferrosomes that contain amorphous iron phosphate biominerals.

FezAB is associated with ferrosomes

To interrogate the mechanism of ferrosome formation, isolated ferrosomes from *fur*::CT cells were subjected to liquid chromatography–tandem mass spectrometry (LC–MS/MS) to identify ferrosome-associated proteins. First, the cell lysates of *fur*::CT before and after ferrosome isolation were directly compared. Mass spectrometry
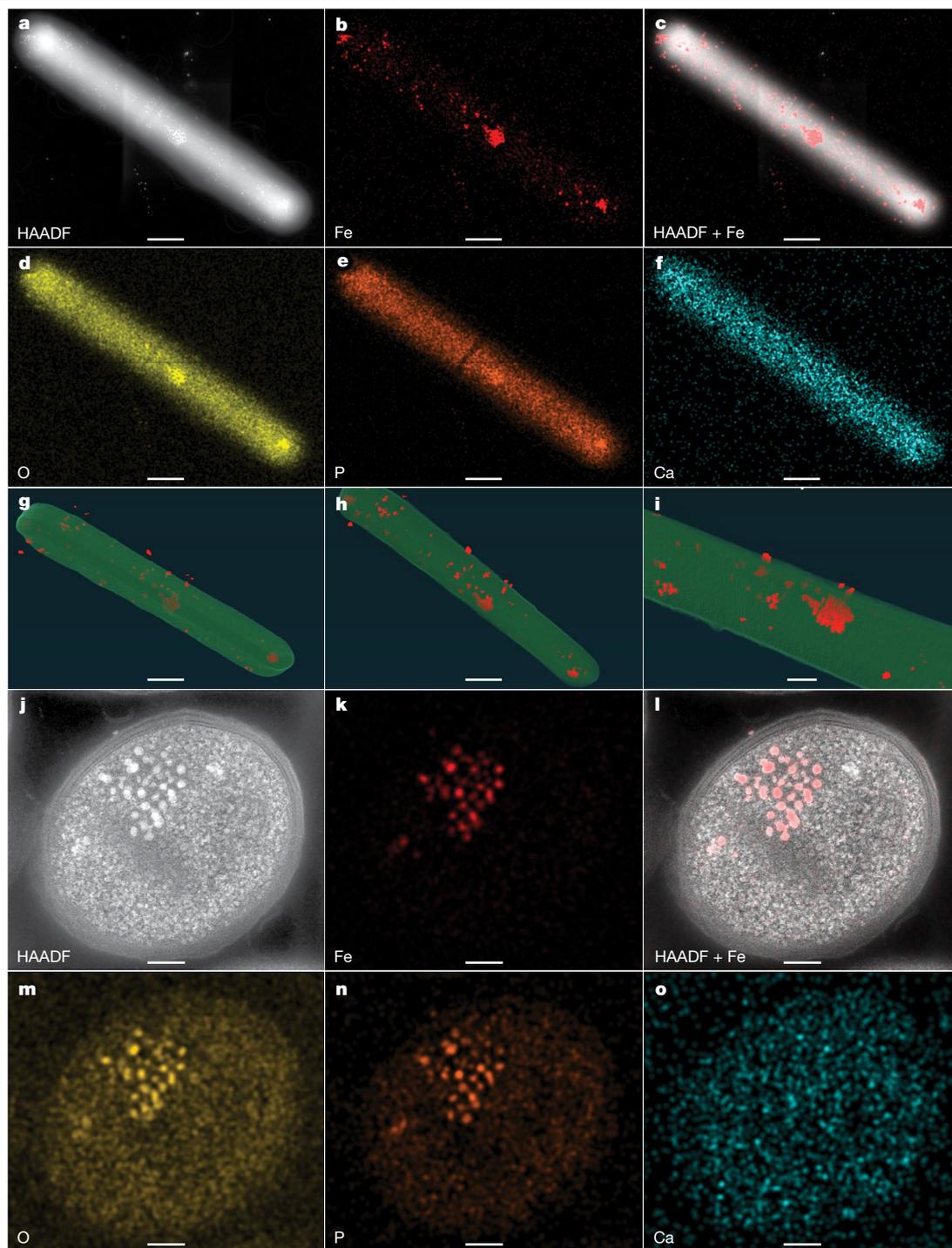
Fig. 3 | STEM–EDS determines the chemical composition of the intracellular electron-dense granules produced by *C. difficile*. a–f, Representative micrographs of a *C. difficile fur*::CT cell by HAADF-STEM imaging (**a**) or EDS maps (**b–f**) of Fe (**b**), HAADF merged with Fe signal (**c**), O (**d**), P (**e**) and Ca (**f**). **g–i**, Three still images of a reconstructed electron tomogram showing electron-dense granules in red. The full video of the reconstructed electron tomograph is in Supplementary Video 1. **j–o**, Representative images of ultrathin sections (100 nm) of the *fur*::CT cells stained with uranyl acetate and processed using a freeze-substitution technique. Images taken by HAADF-STEM (**j**) or EDS maps (**k–o**) of Fe (**k**), HAADF merged with Fe signal (**l**), O (**m**), P (**n**) and Ca (**o**). Scale bars, 500 nm (**a–h**), 100 nm (**i**) and 200 nm (**j–o**). The integrated EDS spectra are shown in Extended Data Fig. 3. **a–f,j–o**, Experiments were conducted at least five times independently with similar results.

analysis showed about 87% reduction of FezA and undetectable levels of FezB in the cell lysates following removal of ferrosomes (Extended Data Fig. 6a,b and Supplementary Table 4), suggesting that the majority of these two proteins are associated with ferrosomes. Indeed, quantitative label-free proteomic analysis showed that both FezA and FezB were highly enriched in the ferrosome fraction (78- and 351-fold,

respectively) (Extended Data Fig. 6c and Supplementary Table 5), compared with the background control of *fur*::CT Δ*fezB*, which does not produce ferrosomes (Fig. 2e,f and Extended Data Fig. 7). However, we were unable to detect FezX from any of these proteomic datasets. Multiple extra runs of targeted proteomics analyses also failed to detect this protein. Altogether, these data demonstrate that both membrane
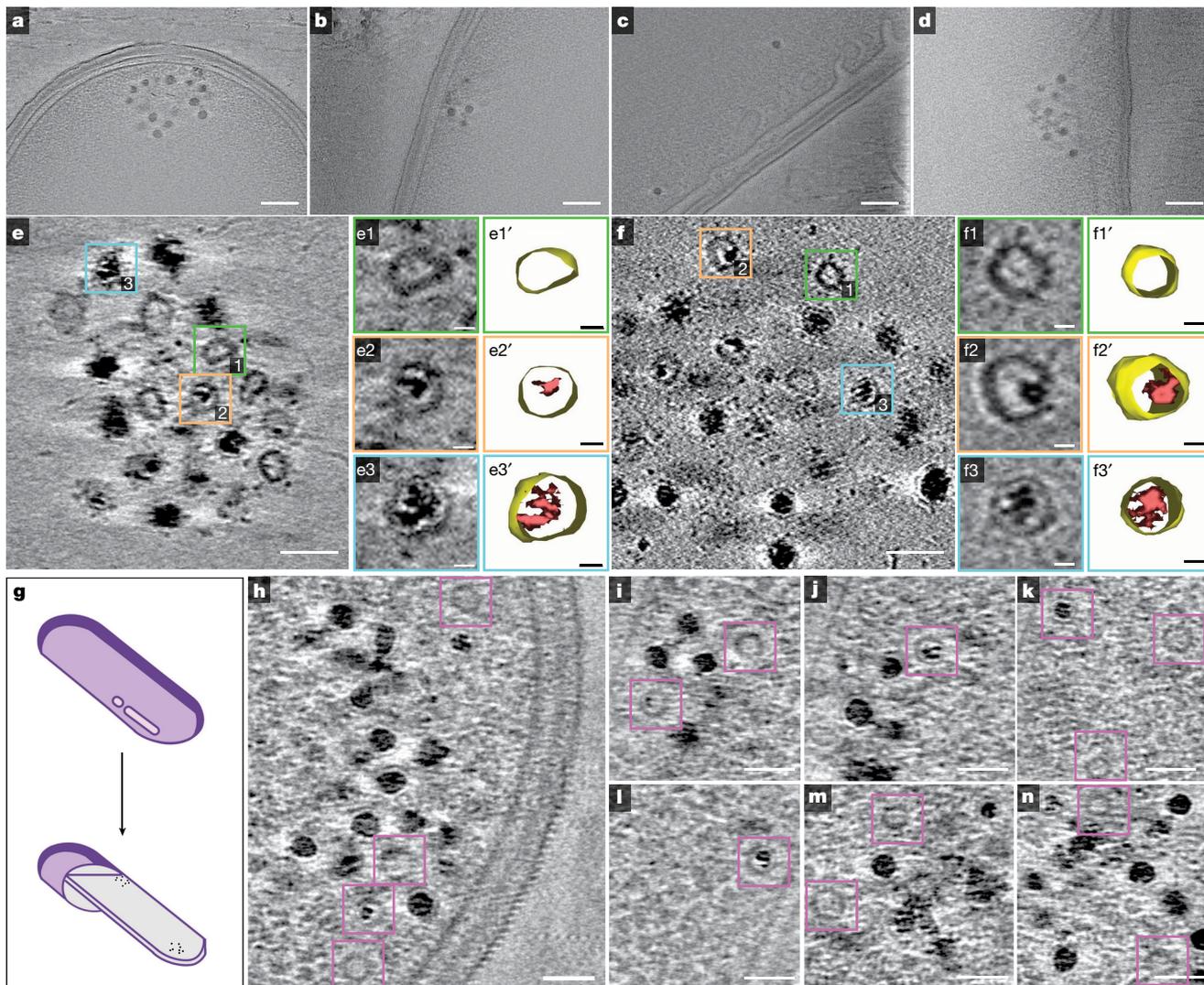
Fig. 4 | Ferrosomes are membrane-bound iron storage organelles visualized by cryo-ET. a–d, Four representative tomographic slices show ferrosome clusters localized in proximity to the cell membranes of intact *fur*::CT cells. The full video of the reconstructed electron tomograms is in Supplementary Video 2. **e,f**, Tomographic slices show that isolated ferrosomes are membrane bound. Boxed areas mark empty vesicles and vesicles filled with varied levels of iron phosphate minerals. Magnified views (**e1–e3, f1–f3**) and 3D segmentation models (**e1'–e3', f1'–f3'**) of membrane vesicles are shown. The full videos of the

reconstructed electron tomograms are in Supplementary Videos 6 and 7. **g**, A schematic of cryo-FIB milling. **h–n**, Seven representative cryo-electron tomographic slices in FIB-milled lamellae (around 200 nm thick) show that ferrosomes are membrane bound. Purple boxes mark empty vesicles and vesicles filled with varied levels of iron phosphate minerals. The full videos of the reconstructed electron tomograms are in Supplementary Videos 8–10. Scale bars, 100 nm (**a–d**), 50 nm (**e,f**), 10 nm (**e1–e3, e1'–e3', f1–f3, f1'–f3'**), 50 nm (**h–n**). FIB, focused ion beam.

proteins, FezA and FezB, are associated with ferrosomes consistent with observations made in *Desulfovibrio magneticus*[8].

Essentiality of the ferrosome system

Heterologous expression of *fez* genes from *S. putrefaciens* and *Rhodopseudomonas palustris* into *Escherichia coli* and *Magnetospirillum magneticum*, respectively, results in ferrosome formation[8]. To further evaluate the sufficiency of *C. difficile* FezAB for ferrosome formation, we heterologously expressed FezAB in *Bacillus subtilis*, which does not encode the *fez* operon. Ferrosomes were not detected under ferrosome-promoting conditions in which iron was added to iron-starved *B. subtilis* cells growing anaerobically (Extended Data Fig. 8a,b), indicating that expression of FezAB alone is not sufficient to produce ferrosomes. We next heterologously expressed the entire *fez* operon including the intergenic region (*fezXAB*) in *B. subtilis*. This strain produced electron-dense granules in cells grown in lysogeny broth rich

medium and significantly more granules were present when these cells were grown under ferrosome-promoting conditions (Extended Data Fig. 8c,d). EDS analysis showed that Fe is the only metal enriched in these granules (Extended Data Fig. 8e–k). These data indicate that the entire *fez* operon is required and sufficient for ferrosome formation.

Membrane-bound iron storage organelles

To investigate whether ferrosomes are localized in membranous compartments, cryo-electron tomography (cryo-ET) of vitrified *C. difficile fur*::CT cells was used. Ferrosome clusters were often found in proximity to the cell membrane of intact cells (Fig. 4a–d and Extended Data Fig. 9a). The reconstructed 3D tomograms of the intact *C. difficile* cells showed that lipid-like membrane vesicles are present within the ferrosome clusters although the resolution was limited due to interference from the cellular content and thickness of the sample (Fig. 4a–d, Extended Data Fig. 9b and Supplementary Videos 2–4).

Article

To better visualize the ferrosome membranes, a ferrosome cluster released from a lysed *fur*::CT cell during the vitrification process was further selected for cryo-ET imaging and 3D reconstruction (Extended Data Fig. 9c). Many membrane vesicles, either empty or partially filled with iron granules, were detected within this ferrosome cluster (Extended Data Fig. 9d and Supplementary Video 5). However, membranes were not detectable around all ferrosomes, particularly for fully loaded ferrosomes, owing to the strong electron scattering of iron particles and resolution limit. Isolated ferrosomes were then imaged by cryo-ET. All imaged ferrosomes were filled with various levels of iron phosphate minerals and evidently bound by a lipid-like membrane (Fig. 4e,f and Supplementary Videos 6 and 7). These data demonstrate that *C. difficile* produces membrane-bound ferrosome organelles consistent with the results obtained from *D. magneticus*[8].

To better visualize ferrosome membrane structures in situ, lamellae (around 200 nm thick) of vitrified *C. difficile fur*::CT cells were prepared using cryo-focused ion beam scanning electron microscopy (cryo-FIB-SEM) and imaged by cryo-ET (Fig. 4g and Extended Data Fig. 9e,f). Seventy-one tomograms of lamellae were obtained and three representative tomograms are shown (Fig. 4h–n and Supplementary Videos 8–10). These data showed that ferrosomes are membrane bound and ferrosome clusters are frequently localized adjacent to the cell membrane (Fig. 4h–n and Supplementary Videos 7 and 8). Further experimentation is required to determine the mechanism by which the ferrosome membranes are formed.

Ferrosomes combat nutritional immunity

The pathogenesis of *C. difficile* is dependent on its ability to acquire nutrient metals for colonization and replication[13–15,29]. To investigate the contribution of ferrosomes to CDI, C57BL/6 mice were infected with WT or Δ*fezB* spores and disease progression was monitored for 4 days postinfection (dpi). Although no germination defects were observed for Δ*fezB* in vitro (Extended Data Fig. 10a), mice infected with Δ*fezB* showed significantly reduced bacterial burden and weight loss relative to mice infected with WT at 4 dpi (Fig. 5a and Extended Data Fig. 10b), indicating that FezB promotes *C. difficile* survival and persistence within the host.

Inflammatory bowel disease (IBD) is associated with *C. difficile* and patients with IBD have an increased risk and higher incidence of CDI compared with the general population[32,33]. This may be in part due to disrupted iron levels in the gastrointestinal tract of patients with IBD[34]. To evaluate the impact of IBD and CDI on metal levels in the gut, stool samples from four groups of human patients were subjected to metal quantification using ICP-MS: patients with IBD negative for *C. difficile*, patients with CDI, patients with both IBD and CDI, and control patients that have no or minimal inflammation in the gut and tested negative for *C. difficile*. Patients with CDI showed significantly lower levels of Fe, Zn and Mn compared with the other three groups (Fig. 5b and Extended Data Fig. 10c,d), suggesting that CDI strongly induces metal dysregulation in the gastrointestinal tract. Additionally, levels of Fe and other metals were significantly higher in patients with IBD compared with non-IBD patients (Fig. 5b and Extended Data Fig. 10c,d), which can be explained by blood loss and reduced iron absorption in the inflamed mucosa of patients with IBD[34]. This motivated us to develop a chemically induced colitis mouse model using dextran sulfate sodium (DSS) to study the importance of ferrosomes to *C. difficile* survival in the presence of severe inflammation that can appear during CDI. The impact of DSS on metal levels in the gut was monitored using ICP-MS before treatment at −7 dpi, during treatment at −4 and −2 dpi, before CDI on day 0 and during CDI elicited by WT spores. Fe levels were significantly elevated after DSS treatment, reduced on day 0 before infection and further decreased at 1 dpi (Fig. 5c). Some minor changes were detected for other metals, but these did not approach the magnitude of the Fe changes (Extended Data Fig. 10e–g). These data demonstrate that nutrient iron levels in the gut are specifically affected by intestinal inflammation and colitis induced through DSS.

We proposed that ferrosomes are important for *C. difficile* to adapt to iron stress in the inflamed gut. To test this, DSS-treated C57BL/6 mice were infected with WT or Δ*fezB* spores. These mice were highly susceptible to CDI, and by 2 dpi most mice lost about 20% of their body weight. Therefore, disease progression was monitored for only 2 d. Δ*fezB* infection showed significantly reduced colonization relative to WT on both 1 and 2 dpi although weight loss was comparable (Fig. 5d and Extended Data Fig. 10h). Both groups of mice treated with DSS showed significantly shorter colons, 53.4 ± 1.7 mm for WT infection and 59.2 ± 2.0 mm for Δ*fezB*-infected mice, compared with untreated mice (74.5 ± 1.7 mm) (Fig. 5e). WT infection led to varying amounts of neutrophilic inflammation in the mucosa and submucosa as well as moderate to marked submucosal oedema, whereas inflammation and submucosal oedema were substantially reduced in Δ*fezB*-infected mice (Fig. 5f,g and Extended Data Fig. 10i). These data demonstrate that FezB is an important factor for *C. difficile* colonization and infection in the inflamed gut.

Levels of iron-sequestering proteins including CP, LCN-2 and lactoferrin were monitored in the DSS-treated mice. On day 0 before infection, levels of all three proteins were drastically elevated compared with −7 dpi, indicating that severe inflammation is induced by DSS and present in the intestine during the onset of CDI. Significantly reduced levels of CP and lactoferrin were observed in Δ*fezB*-infected mice compared with WT-infected mice on both 1 and 2 dpi (Fig. 5h and Extended Data Fig. 10j,k), which is consistent with the lower bacterial burden during Δ*fezB* infection (Fig. 5d). The spatial distribution of CP (S100A8) was visualized in the infected murine caecum tissue using imaging mass spectrometry (IMS) and S100A8 was found to be abundant within the submucosal and mucosal layers but not the muscularis externa of the distal colon (Fig. 5i–l and Extended Data Fig. 10l). Interestingly, in the Δ*fezB*-infected mice, CP levels were lower at 1 dpi compared with 0 dpi whereas no significant difference was observed in WT-infected mice (Fig. 5h), suggesting that the contribution of FezB to *C. difficile* pathogenesis may be particularly important in response to CP-mediated nutrient metal limitation.

Next, the impact of CP on transcription of *fezXAB* was evaluated using qPCR. Expression of *fezXAB* is upregulated following the treatment of purified CP compared with a vehicle control in vitro (Fig. 5m). Transcriptional activation of *fezXAB* in vivo during CDI was further examined in C57BL/6 WT and CP deficient (*S100a9*^{−/−}) mice. All three genes (*fezXAB*) showed higher messenger RNA levels in the caecal samples of WT mice compared with growth in vitro, but this activation was significantly diminished in *S100a9*^{−/−} mice (Fig. 5n), indicating that CP-mediated iron sequestration is the major contributor to ferrosome activation during CDI. To evaluate the importance of ferrosomes in overcoming CP-dependent nutritional immunity during CDI, *S100a9*^{−/−} mice were infected with either WT or Δ*fezB* spores and disease progression was monitored for 2 d. No differences were observed between the two groups for either colonization or weight loss (Fig. 5o and Extended Data Fig. 10m), indicating that the ferrosome system is not required for CDI when the major iron sequestration protein CP is absent. Collectively, this study demonstrates that the ferrosome system (*fezXAB*) is required and sufficient for the formation of the membrane-bound ferrosome organelles in *C. difficile*, and ferrosomes serve as an iron storage mechanism to alleviate iron overload and oxidative stress. The ferrosome system is activated in vivo during CDI to compete with nutritional immunity and is important for *C. difficile* colonization in a CP-dependent manner.

Discussion

The ferritin superfamily proteins have long been appreciated to be the major iron storage mechanism in all kingdoms of life for which
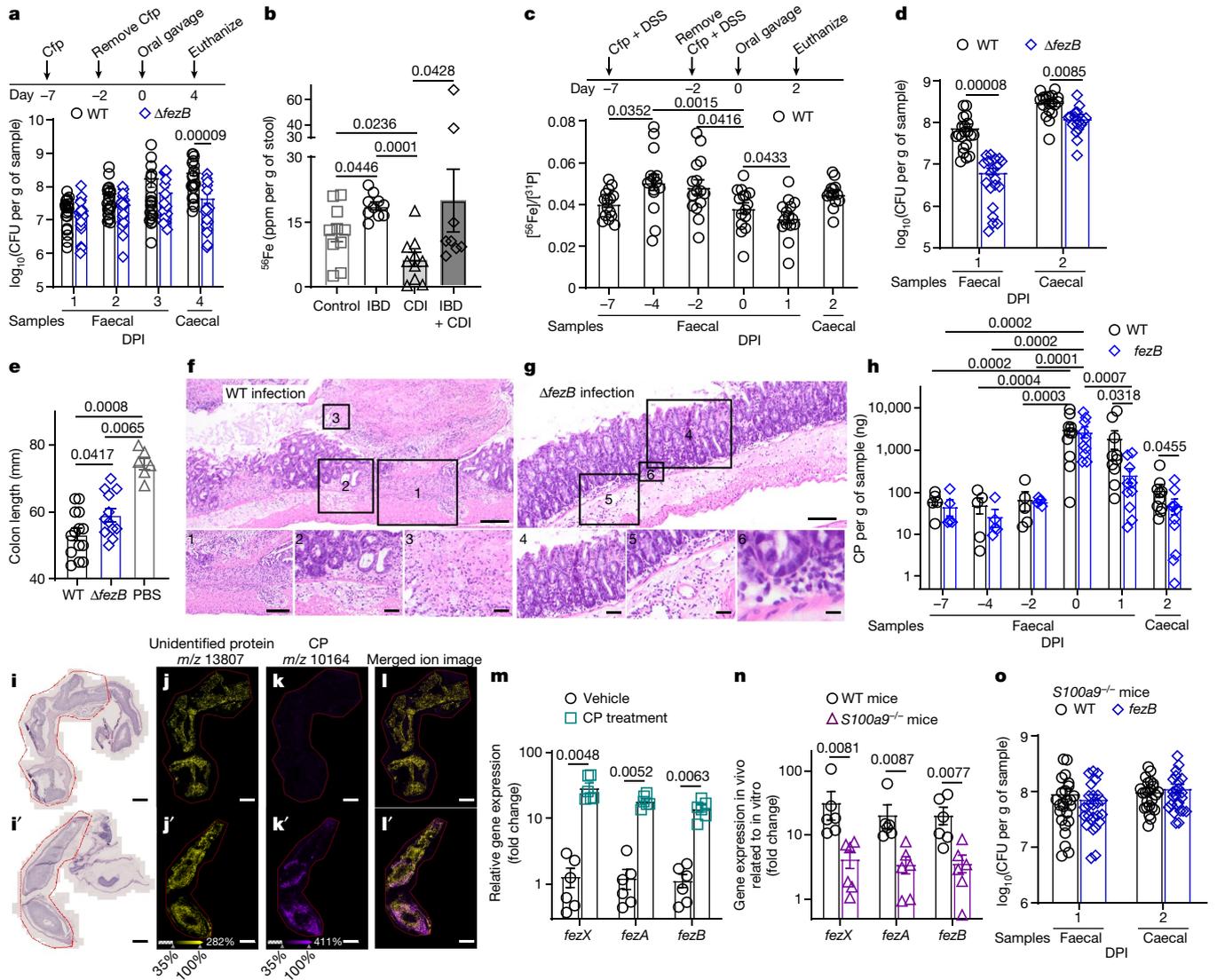
Fig. 5 | *C. difficile* ferrosomes circumvent CP-mediated iron sequestration.
a, CFUs of C57BL/6J mice infected with WT or Δ*fezB* spores (*n* = 20). **b**, Fe levels were quantified by ICP-MS in stools. Data are expressed as ppm per gram of stools, *n* = 10 for all groups except IBD + CDI (*n* = 8). **c**–**h**, Infection studies were conducted using mice pretreated with both Cfp and DSS for 5 d. **c,d**, Fe levels (**c**) (*n* = 10) and CFUs (**d**) (*n* = 20) were monitored. **e**, Colon lengths of mice were quantified at 2 dpi (*n* = 10). **f,g**, Representative photomicrographs of H&E-stained colon slides infected with WT (**f**) or Δ*fezB* (**g**). **f**, A 'volcano' lesion from a mouse infected with WT. Inset 1, ulceration of the mucosa; inset 2, neutrophils and oedema; inset 3, fibrin and necrosis. **g**, Murine colon infected with Δ*fezB* showing unaffected mucosa (inset 4) and neutrophilic inflammation in the mucosa (insets 5 and 6). Scale bars, 100 μm (inset 1, 100 μm; insets 2, 4, 5, 50 μm; insets 3, 6, 20 μm). **h**, CP levels were quantified and presented as mean ± s.e.m. (*n* = 10). **i**–**l**, Distribution of CP in colons examined using matrix-assisted laser desorption/ionization (MALDI)-IMS of *S100a9*^{−/−} (**i**–**l**) or C57BL/6J (**i′**–**l′**) mice infected with WT spores. **i,i′**, H&E staining of murine colons. Red outlines indicate areas sampled for IMS. MALDI-IMS ion images of an unidentified protein (yellow) (**j,j′**), CP (purple) (**k,k′**) or merged (**l,l′**). Scale bars, 1,000 μm. **m,n**, Expression of *fezXAB* was quantified by qPCR in vitro (**m**) and in vivo (**n**). Data are presented as mean ± s.e.m. (*n* = 6). **o**, CFUs of *S100a9*^{−/−} mice infected with WT or Δ*fezB* spores (*n* = 25). Data are mean ± s.e.m. **f,g,i**–**l,i′**–**l′**, Experiments were conducted twice independently with similar results. Statistical analyses used two-way ANOVA (**a,h**), one-way ANOVA (**b**–**c,e**) or two-tailed *t*-tests (**d,m**–**o**) and *P* values are denoted. Cfp, cefoperazone; CFU, colony forming units; H&E, haematoxylin and eosin.

cellular iron is stored within a protein nanocage[35,36]. In addition to ferritin-mediated iron storage, we report here that the human pathogen *C. difficile* stores iron as iron phosphate minerals inside membrane-bound ferrosome organelles. Ferrosomes may represent a common strategy used by anaerobes to occupy specific niches during iron stress in natural environments, as shown previously[8,37,38], and within the mammalian host as demonstrated in this study. Whereas ferrosomes promote growth on iron starvation in *S. putrefaciens*[8], they protect *C. difficile* against iron intoxication during transient iron overload (Fig. 1), suggesting that the role of ferrosomes in iron metabolism is affected by the ecological niche inhabited by bacteria. It is

possible that ferrosomes have evolved in gastrointestinal pathogens to enable survival in the presence of the severe flux in iron concentration experienced in the gut. Understanding the biological process of ferrosome formation is still in its infancy. Although the P_{1B6}-ATPase FezB is well conserved in diverse species, the size of the gene clusters differs, ranging from three genes in both *C. difficile* (*fezXAB*) and *D. magneticus* RS-1 (*fezABC*), to six in both *S. putrefaciens* CN-32 and *R. palustris* CGA009 (*fezBCDEFG*), to eight in *Thioflavicoccus mobilis*[8]. This implies that the molecular basis underlying ferrosome formation may differ among species. Induction of the ferrosome system (*fezXAB*) driven by an IPTG (isopropyl β-ᴅ-1-thiogalactopyranoside)-inducible

Article

promoter is sufficient for ferrosome formation in the heterologous *B. subtilis* host; however, ferrosome production in this system is enhanced when iron concentrations are altered (Extended Data Fig. 8). These data suggest that other factors are involved in ferrosome biogenesis, which may include factors involved in iron trafficking from the cytosol to ferrosomes, membrane vesicle formation, iron oxidation, biomineralization or ferrosome-stored iron release. FezA, FezB and several other proteins are associated with ferrosomes (Extended Data Fig. 6 and Supplementary Tables 4 and 5) and ferrosomes are often found in proximity to the cell membrane (Fig. 4), leading to the possibility that there is an association between ferrosome membrane and cellular membrane. Further studies are underway to elucidate how these proteins are specifically sorted into ferrosome membrane vesicles and what physiological roles they play in ferrosome biogenesis. Nonetheless, the ferrosome nanoparticles have the potential to redefine the concept of trace element storage in anaerobes, unveil important insight into how gut microorganisms cope with changes in elemental levels within the hosts and provide a prototype for production of metal nanoparticles and drug delivery vesicles, and other bionanotechnology applications. Finally, the importance of ferrosome formation to combat host-imposed nutritional immunity establishes ferrosome formation as a new target for the development of antimicrobial therapeutics for the treatment of infection caused by anaerobic bacteria.

Online content

Any methods, additional references, Nature Portfolio reporting summaries, source data, extended data, supplementary information, acknowledgements, peer review information; details of author contributions and competing interests; and statements of data and code availability are available at https://doi.org/10.1038/s41586-023-06719-9.

1. Pi, H. & Helmann, J. D. Ferrous iron efflux systems in bacteria. *Metallomics* **9**, 840–851 (2017).
2. Imlay, J. A. Pathways of oxidative damage. *Annu. Rev. Microbiol.* **57**, 395–418 (2003).
3. Chandrangsu, P., Rensing, C. & Helmann, J. D. Metal homeostasis and resistance in bacteria. *Nat. Rev. Microbiol.* **15**, 338–350 (2017).
4. Imlay, J. A. The mismetallation of enzymes during oxidative stress. *J. Biol. Chem.* **289**, 28121–28128 (2014).
5. Sheldon, J. R. & Heinrichs, D. E. Recent developments in understanding the iron acquisition strategies of Gram positive pathogens. *FEMS Microbiol. Rev.* **39**, 592–630 (2015).
6. Sheldon, J. R., Laakso, H. A. & Heinrichs, D. E. Iron acquisition strategies of bacterial pathogens. *Microbiol. Spectr.* https://doi.org/10.1128/microbiolspec.VMBF-0010-2015 (2016).
7. Lessa, F. C. et al. Burden of *Clostridium difficile* infection in the United States. *N. Engl. J. Med.* **372**, 825–834 (2015).
8. Kelly, C. P. & LaMont, J. T. *Clostridium difficile*—more difficult than ever. *N. Engl. J. Med.* **359**, 1932–1940 (2008).
9. Janka, J. & O'Grady, N. P. *Clostridium difficile* infection: current perspectives. *Curr. Opin. Crit. Care* **15**, 149–153 (2009).
10. Rupnik, M., Wilcox, M. H. & Gerding, D. N. *Clostridium difficile* infection: new developments in epidemiology and pathogenesis. *Nat. Rev. Microbiol.* **7**, 526–536 (2009).
11. Palmer, L. D. & Skaar, E. P. Transition metals and virulence in bacteria. *Annu. Rev. Genet.* **50**, 67–91 (2016).
12. Hood, M. I. & Skaar, E. P. Nutritional immunity: transition metals at the pathogen–host interface. *Nat. Rev. Microbiol.* **10**, 525–537 (2012).
13. Bullen, J. J. The significance of iron in infection. *Rev. Infect. Dis.* **3**, 1127–1138 (1981).
14. Cassat, J. E. & Skaar, E. P. Iron in infection and immunity. *Cell Host Microbe* **13**, 509–519 (2013).
15. Parrow, N. L., Fleming, R. E. & Minnick, M. F. Sequestration and scavenging of iron in infection. *Infect. Immun.* **81**, 3503–3514 (2013).
16. Nakashige, T. G., Zhang, B., Krebs, C. & Nolan, E. M. Human calprotectin is an iron-sequestering host-defense protein. *Nat. Chem. Biol.* **11**, 765–771 (2015).
17. Corbin, B. D. et al. Metal chelation and inhibition of bacterial growth in tissue abscesses. *Science* **319**, 962–965 (2008).
18. Moschen, A. R., Adolph, T. E., Gerner, R. R., Wieser, V. & Tilg, H. Lipocalin-2: a master mediator of intestinal and metabolic inflammation. *Trends Endocrinol. Metab.* **28**, 388–397 (2017).
19. Kell, D. B., Heyden, E. L. & Pretorius, E. The biology of lactoferrin, an iron-binding protein that can help defend against viruses and bacteria. *Front. Immunol.* **11**, 1221 (2020).
20. McCormick, A. et al. NETs formed by human neutrophils inhibit growth of the pathogenic mold *Aspergillus fumigatus*. *Microbes Infect.* **12**, 928–936 (2010).
21. Urban, C. F. et al. Neutrophil extracellular traps contain calprotectin, a cytosolic protein complex involved in host defense against *Candida albicans*. *PLoS Pathog.* **5**, e1000639 (2009).
22. Deriu, E. et al. Probiotic bacteria reduce *Salmonella typhimurium* intestinal colonization by competing for iron. *Cell Host Microbe* **14**, 26–37 (2013).
23. Bianchi, M., Niemiec, M. J., Siler, U., Urban, C. F. & Reichenbach, J. Restoration of anti-Aspergillus defense by neutrophil extracellular traps in human chronic granulomatous disease after gene therapy is calprotectin-dependent. *J. Allergy Clin. Immunol.* **127**, 1243–1252 e1247 (2011).
24. Ayling, R. M. & Kok, K. Fecal calprotectin. *Adv. Clin. Chem.* **87**, 161–190 (2018).
25. Barbut, F. et al. Faecal lactoferrin and calprotectin in patients with *Clostridium difficile* infection: a case–control study. *Eur. J. Clin. Microbiol. Infect. Dis.* **36**, 2423–2430 (2017).
26. He, T. et al. Fecal calprotectin concentrations in cancer patients with *Clostridium difficile* infection. *Eur. J. Clin. Microbiol. Infect. Dis.* **37**, 2341–2346 (2018).
27. Zackular, J. P. et al. Dietary zinc alters the microbiota and decreases resistance to *Clostridium difficile* infection. *Nat. Med.* **22**, 1330–1334 (2016).
28. Ho, T. D. & Ellermeier, C. D. Ferric uptake regulator Fur control of putative iron acquisition systems in *Clostridium difficile*. *J. Bacteriol.* **197**, 2930–2940 (2015).
29. Grant, C. R. et al. Distinct gene clusters drive formation of ferrosome organelles in bacteria. *Nature* **606**, 160–164 (2022).
30. McAllister, K. N., Bouillaut, L., Kahn, J. N., Self, W. T. & Sorg, J. A. Using CRISPR-Cas9-mediated genome editing to generate *C. difficile* mutants defective in selenoproteins synthesis. *Sci. Rep.* **7**, 14672 (2017).
31. Byrne, M. E. et al. *Desulfovibrio magneticus* RS-1 contains an iron- and phosphorus-rich organelle distinct from its bullet-shaped magnetosomes. *Proc. Natl Acad. Sci. USA* **107**, 12263–12268 (2010).
32. Nitzan, O., Elias, M., Chazan, B., Raz, R. & Saliba, W. *Clostridium difficile* and inflammatory bowel disease: role in pathogenesis and implications in treatment. *World J. Gastroenterol.* **19**, 7577–7585 (2013).
33. Sinh, P., Barrett, T. A. & Yun, L. *Clostridium difficile* infection and inflammatory bowel disease: a review. *Gastroenterol. Res. Pract.* **2011**, 136064 (2011).
34. Wiskin, A. E., Fleming, B. J., Wootton, S. A. & Beattie, R. M. Anaemia and iron deficiency in children with inflammatory bowel disease. *J. Crohns Colitis* **6**, 687–691 (2012).
35. Bou-Abdallah, F. The iron redox and hydrolysis chemistry of the ferritins. *Biochim. Biophys. Acta Gen. Subj.* **1800**, 719–731 (2010).
36. Hintze, K. J. & Theil, E. C. Cellular regulation and molecular interactions of the ferritins. *Cell. Mol. Life Sci.* **63**, 591 (2006).
37. Glasauer, S., Langley, S. & Beveridge, T. J. Intracellular iron minerals in a dissimilatory iron-reducing bacterium. *Science* **295**, 117–119 (2002).
38. Glasauer, S. et al. Mixed-valence cytoplasmic iron granules are linked to anaerobic respiration. *Appl. Environ. Microbiol.* **73**, 993–996 (2007).

Methods

Bacterial strains and growth conditions

All strains and plasmids used in this study are listed in Supplementary Table 2. *C. difficile* CD196 WT strain and derivatives were grown in an anaerobic chamber (90% nitrogen, 5% hydrogen, 5% carbon dioxide, Coy Lab Products) in brain–heart-infusion broth (BD Life Sciences) supplemented with 0.5% yeast extract (BD Life Sciences) (BHIS) and 0.1% cysteine (Sigma-Aldrich) or solid BHIS agar plates at 37 °C with appropriate antibiotic selection. *E. coli* and *B. subtilis* strains were grown in lysogeny broth or lysogeny broth agar plates with appropriate antibiotic selection. The concentrations of antibiotics used were: carbenicillin (50 µg ml^{-1}), thiamphenicol (20 µg ml^{-1}), chloramphenicol (2.5 µg ml^{-1}), kanamycin (50 µg ml^{-1}), lincomycin (20 µg ml^{-1}) and tetracycline (5 µg ml^{-1}).

Plasmid construction

The *C. difficile fezB*-targeted CRISPR plasmid was constructed by amplifying 500 bp upstream and downstream from the *fezB* gene using primer pairs fezB_upstream_fwd/fezB_upstream_rev and fezB_downstream_fwd/fezB_downstream_rev, respectively. The fragments were cloned into the NotI and XhoI sites of pKM197 using Gibson assembly. The *fezB*-targeting guide RNA (gRNA) along with gRNA scaffold sequence was synthesized (fezB_gRNA_gblock) and inserted into the KpnI and MluI sites by Gibson assembly. The resulting plasmid (pKM197-*fezB*) was transformed into *E. coli* DH5α, confirmed by Sanger sequencing and transformed into *E. coli* MG1655 to generate multimers of the plasmid, which enhances conjugation efficiency. The transformants were validated by restriction digestion using BsrGI and BamHI and subsequently transformed into *B. subtilis* JH BS2 which harbours a Tn916 conjugation system. The plasmid (pKM197-*fezB*) was then transferred to *C. difficile* WT or *fur*::CT through conjugation using *B. subtilis* JH BS2 pKM197-*fezB* as a donor, further confirmed by colony PCR using primers listed in Supplementary Table 3. Positive clones were passed up to four times on 1% xylose plates to induce the CRISPR–Cas9 system and colonies were screened by colony PCR using one primer pair located outside *fezB*: fezB_ck2_fwd/fezB_ck2_rev and another primer pair located inside *fezB*: fezB_ck_fwd/fezB_ck_rev. After confirmation of *fezB* deletion, the plasmid pKM197-*fezB* was then cured by ten passages in BHIS medium containing 0.5% xylose. Deletion of *fezB* was further confirmed by Sanger sequencing and whole genome sequencing. A complete list of oligonucleotides used in this study is in Supplementary Table 3.

For *C. difficile* Δ*fezB* complementation plasmids, the *fezB* gene and its promoter region were inserted by Gibson assembly into the NotI and XhoI sites of pJS116. The resulting plasmid (pJS116-*fezB*) was transformed into *E. coli* DH5α, confirmed by Sanger sequencing and then transformed into *E. coli* MG1655. The transformants were validated by restriction digestion using BsrGI and BamHI and subsequently transformed into *B. subtilis* JH BS2. The plasmid (pJS116-*fezB*) was then transferred to *C. difficile* WT through conjugation using *B. subtilis* JH BS2 pJS116-*fezB* as a donor, further confirmed by colony PCR using primers listed in Supplementary Table 3.

5′ RACE

To determine the transcription start sites of the *fez* operon, 5′ RACE was carried out using a 5′/3′ RACE Kit following the manufacturer's instructions (Sigma, Cat. no. 03353621001). Briefly, total RNA was isolated from *C. difficile* WT strain using an RNeasy RNA isolation kit (Qiagen). Then, 800 ng of total RNA was used to synthesize the first-strand cDNA using a gene-specific primer (fezA_SP1_RACE or fezA_SP2_RACE; Supplementary Table 3). The resulting cDNA was purified using a gel extraction purification kit (Qiagen) and a 3′-poly(A) tail was added using recombinant terminal transferase and dATP. Two runs of nested PCR were then carried out using PCR anchor primer and gene-specific primers listed in Supplementary Table 3. PCR products were separated by gel electrophoresis and the transcription start sites were identified using Sanger sequencing.

RNA extraction and qPCR

In vitro RNA isolation. To define the regulation mechanism of the *fez* genes (*fezXAB*) by the regulator Fur (Fig. 1b), *C. difficile* strains (WT and *fur*::CT) were grown overnight anaerobically in BHIS medium at 37 °C, subcultured at a 1:50 ratio into fresh BHIS medium and grown to cell density (OD$_{600}$) of 0.4–0.6. To check the effects of iron limitation on transcription of these genes (Fig. 1c), 100 µM dipyridyl or an equal volume of 0.1 M NaOH (vehicle) was added to WT cell culture (OD$_{600}$ ≈ 0.4) and incubated for a further 30 min. To check the transcription changes of *fezxAB* on CP treatment (Fig. 5m), 350 µg ml^{-1} CP or an equal volume of buffer (20 mM Tris pH 7.5, 100 mM NaCl, 10 mM β-mercaptoethanol and 3 mM CaCl$_2$) was added to WT cell culture (OD$_{600}$ ≈ 0.4) and incubated for a further 30 min. Aliquots of 2 ml of cell culture were collected by centrifugation. Cells were lysed using lysing matrix A tubes (MP Biomedicals) and a bead beater. Total RNA was extracted using an RNeasy Mini Kit (Qiagen) following the manufacturer's instructions. Each RNA sample was eluted with 60 µl of RNase-free water.

In vivo RNA isolation. C57BL/6J WT mice or *S100a9*$^{-/-}$ mice were infected with *C. difficile* WT spores as described in the 'Animal models' section. Mice were euthanized at 2 dpi, and their caecal contents were collected and homogenized using lysing matrix A tubes (MP Biomedicals) and a bead beater. RNA was isolated using the RNeasy PowerMicrobiome kit (Qiagen) according to the manufacturer's instructions. Each RNA sample was eluted with 50 µl of RNase-free water.

All RNA samples were treated with Turbo-DNA free DNase (Ambion) and quantified using a NanoDrop spectrophotometer. We subjected 200 ng of total RNA from each sample to cDNA synthesis using high-capacity cDNA reverse transcription kits (Applied Biosystems). Primers used in this study are listed in Supplementary Table 3. qPCR was then conducted using iQ SYBR green supermix (Bio-Rad) on a CFX96 qPCR cycler (Bio-Rad). The housekeeping gene *rpoB* was used as an internal control.

Growth curves

For growth curves included in Fig. 1d and Extended Data Fig. 1, *C. difficile* strains were grown overnight anaerobically in BHIS medium at 37 °C, subcultured at a 1:50 ratio into fresh BHIS medium, grown to cell density (OD$_{600}$) of 0.4–0.6 and inoculated at a 1:50 ratio into fresh BHIS medium amended with various treatments as indicated. For growth curves included in Fig. 1e, *C. difficile* strains were grown overnight anaerobically in BHIS medium at 37 °C in the presence of 100 µM dipyridyl and inoculated at a 1:50 ratio into fresh BHIS medium amended with 100 µM dipyridyl and 1 mM FeSO$_4$. Cell growth (OD$_{600}$) was then monitored every 30 min for 24 h at 37 °C anaerobically with continuous shaking using a BioTek Epoch2 spectrophotometer. Experiments were conducted at least three times with three biological replicates each time. Data shown are averages of three biological replicates (mean ± s.d.).

Quantification of intracellular metals by ICP-MS

To quantify intracellular elemental levels in bacterial cultures (Fig. 1f and Extended Data Fig. 2), overnight cultures of *C. difficile* strains were diluted with a ratio of 1:50 into fresh BHIS amended with various treatments as indicated. Cultures were incubated at 37 °C and aliquots of 4 ml of cell cultures were collected at different timepoints as indicated and washed three times with 1 × PBS. To determine elemental levels in human stool samples (Fig. 5b and Extended Data Fig. 10c,d), the mass of each sample was measured in pre-weighed tubes. To determine elemental levels in mouse faecal or caecal samples (Fig. 5c and Extended

Article

Data Fig. 10e–g), samples were collected at different timepoints during infection as indicated. Each sample (bacterial pellet, human stool sample, or mouse faecal or caecal sample) was resuspended in 200 µl of nitric acid and 50 µl of 30% trace metal grade hydrogen peroxide and incubated at 65 °C overnight for digestion. Metal-free tubes and pipette tips were used for all the procedures to avoid contamination. UltraPure H_2O (2 ml) was added to the mixture which was then subjected to elemental quantification using an Agilent 7700 ICP-MS attached to a Teledyne CETAC Technologies ASX-560 autosampler. Elemental data were normalized to the concentration of sulfur or phosphorus, or sample mass, as indicated.

TEM, STEM and STEM–EDS

TEM, STEM and STEM–EDS were performed using a Tecnai Osiris TEM-STEM operating at 200 kV equipped with the Super-X quad EDS detection system. Drift-corrected maps were collected using Bruker Esprit 1.9 with a probe current on the order of 0.5 nA. Ferrosome parameters were quantified by ImageJ using both isolated ferrosomes and ferrosomes inside *C. difficile* cells. EDS spectra were acquired under the HAADF-STEM mode using the Super-X quad EDS detector.

Tilt electron tomography

Bacterial cells were collected, washed three times using 0.1 M HEPES buffer (pH 7.0), deposited onto a carbon-coated copper grid, fixed with 2.5% glutaraldehyde in 0.1 M HEPES for 10 min and washed three times with H_2O. The air-dried grid was then loaded onto a Fischione model 2020 tomography holder. A representative cell was located and STEM–EDS was first performed to confirm the identification of the ferrosomes, allowing the tilt series to be collected simply using *z*-contrast. HAADF-STEM images were collected from −60° to 60° at 1° increments. An automated tilt series was collected using a Tecnai Osiris TEM-STEM operating at 200 kV. The tilt series was then aligned and reconstructed using the simultaneous iterative reconstruction technique (SIRT) method in Inspect 3D. The reconstructed volumes were then rendered and colourized using Amira 2021.

Freeze-substitution

C. difficile fur::CT cells in mid-logarithmic phase ($OD_{600} \approx 0.6$) were collected, washed three times in 0.1 M HEPES buffer (pH 7.0) and fixed with 2.5% glutaraldehyde in 0.1 M HEPES buffer for 30 min. The samples were pelleted into molten low-melt agarose at 30 °C to encapsulate the samples and facilitate handling of bacterial pellets in subsequent steps. The samples were slowly transitioned into 30% glycerol as a cryoprotectant over 24 h at 4 °C and vitrified by plunge-freezing in liquid ethane at −180 °C. Freeze-substitution was carried out in 1.5% uranyl acetate in absolute methanol at −90 °C for 48 h followed by infiltration with HM20 Lowicryl resin over the course of 48 h at −30 °C. The resin was ultraviolet polymerized for 48 h at −30 °C followed by 24 h at 0 °C. During the entire freeze-substitution process the samples were kept in a nitrogen or CO_2 atmosphere. Sections were cut at a nominal thickness of 100 nm using a Leica UC7 ultramicrotome, collected onto carbon-coated Ni grids and stained with lead citrate for 2 min.

Ferrosome isolation

The *C. difficile fur*::CT strain was grown overnight anaerobically in BHIS medium at 37 °C, subcultured at a 1:50 ratio into fresh BHIS medium and grown to cell density (OD_{600}) of around 1. Cells were collected, washed with 50 mM Tris buffer pH 8.0 and resuspended in ice-cold lysis buffer (10 mM Tris pH 8.0, 50 mM NaCl, 1 mM EDTA and 250 mM sucrose) amended with EDTA-free protease inhibitor cocktail. Cells were then lysed by sonication. Cell lysates were clarified by centrifugation, layered over a 65% sucrose cushion and centrifuged at 35,000 rpm for 2 h at 10 °C. The resulting ferrosome pellet was washed twice with 50 mM Tris buffer pH 8.0 and resuspend in 50 µl of 50 mM Tris buffer pH 8.0.

Identification of ferrosome-associated proteins using LC–MS/MS

To identify ferrosome-associated proteins, two sets of LC–MS/MS analyses were conducted: (1) comparison between the cell lysates of *fur*::CT before and after ferrosome isolation, and (2) comparison between the isolated ferrosomes from *fur*::CT cells and the background control (*fur*::CT Δ*fezB*). Cell lysates and isolated ferrosomes were prepared as described above and LC–MS/MS analyses were performed in the University of South Florida Proteomics Core facility. The samples were digested with Trypsin/Lys-C overnight at 37 °C. The subsequent peptides were extracted using 50/50 acetonitrile (ACN)/H_2O/0.1% formic acid, dried in a vacuum concentrator (Labconco) and resuspended in 98% H_2O/2% ACN/0.1% formic acid for LC–MS/MS analysis. The peptides were then separated using a 50 cm C18 reversed-phase HPLC column (Thermo) on an Ultimate3000 UHPLC (Thermo) with a 120 min gradient (2–32% ACN with 0.1% formic acid) and analysed on a hybrid quadrupole-Orbitrap mass spectrometer (Q Exactive Plus, Thermo Fisher Scientific) using data-dependent acquisition in which the top ten most abundant ions are selected for tandem mass spectrometry analysis. Experiments were conducted in triplicate. Raw data files were processed in MaxQuant (www.maxquant.org) and searched against the protein sequence database of *C. difficile* CD196 (UniProt UP000002068). Search parameters included constant modification of cysteine by carbamidomethylation and the variable modification, methionine oxidation. Proteins were identified using the filtering criteria of 1% protein and peptide false discovery rate. For each dataset, the filtered data were normalized across all samples using a label-free quantification method[39]. All proteins identified are listed in Supplementary Tables 4 and 5.

Sample vitrification for cryo-electron tomography

Both *C. difficile* intact cells and isolated ferrosomes were vitrified by plunge-freezing using a Vitrobot Mark III (Thermo Fisher Scientific). Before plunge-freezing, all electron microscopy grids (Quantifoil, Cu R2/2 200 mesh) were glow discharged for 20 s in a glow discharge cleaning system (EMS 100). To prepare intact *C. difficile* cells for cryo-electron tomography (cryo-ET) or FIB milling, 4 µl of cell suspension ($OD_{600} \approx 7$) was added onto an electron microscopy grid, the air-dried grid was then mounted to the plunge freezer and another 4 µl of cell suspension was applied to the same grid right before rapid vitrification using liquid ethane. The parameters of the plunge freezer were set as follows: humidity 100%; temperature 22 °C; blot time: 5 or 3.5 s for cryo-ET or cryo-FIB milling, respectively; blot totals 1; blot offset −1.5; and wait time 10 s. To prepare isolated ferrosomes for cryo-EM, an empty grid was mounted to the plunge freezer, 4 µl of ferrosome suspension was added to the mounted grid in the Vitrobot chamber and the loaded grid was then plunged into liquid ethane for rapid vitrification. The parameters of the plunge freezer were set as follows: humidity 100%; temperature 4 °C; blot time 3.5 s; blot total 1; blot offset −1.5; and wait time 10 s. All the frozen grids were stored in the liquid nitrogen Dewar until use.

Lamella preparation by FIB milling

Cryo-ET lamellae (200 nm thick) of *C. difficile* cells were prepared using a Thermo Fisher Helios G3 CX cryo-FIB-SEM equipped with a Quorum PP3010T cryo-preparation system (Helios, Thermo Fisher Scientific) following a modified procedure[40]. Vitrified samples were loaded onto a 45° pre-tilt TEM grid shuttle under liquid nitrogen and vacuum transferred into the Quorum preparation chamber, which was set to −175 °C. Before insertion into the cryo-FIB-SEM, the sample was sputter-coated with metallic Pt (20 s, 10 mA), and then loaded into the FIB via an airlock, in which a coating of organometallic Pt was deposited using the GIS system (about 8 s at a WD of 6 mm) followed by a 30 s low-magnification exposure to the ion beam set to 1 nA. Lamellae were then milled using consecutively lower ion beam

currents (0.2 nA down to 0.2 pA) with a starting stage tilt angle of 23° and final polish tilt angle of 18°. Expansion joints were milled in parallel with the initial rough mill, whereas the polishing step was performed on all lamellae immediately before sample unloading. Additionally, the lamella width was reduced at each milling step to improve final lamella stability. Samples were then vacuum transferred to liquid nitrogen and stored under liquid nitrogen.

Cryo-ET and data processing

Batch tilt series were collected automatically with Thermo Fisher Tomography5 software on a Thermo Fisher Titan Krios G4 equipped with the Gatan K3 camera or Thermo Fisher Glacios equipped with the Falcon 4 camera. Grids with vitrified samples (isolated ferrosomes, intact *C. difficile* cells or FIB-milled lamellae) were loaded to the cryo-electron microscope with an autoloader and cryo-ET was performed. The tilt series were collected using a dose-symmetric scheme starting from 0° to ±60° with an interval of 2°, defocus value at around −8 or −10 μm, and total electron dosage of approximately 120 e−/Å². After imaging, the tilt series were aligned and reconstructed using IMOD[41] or AreTomo[42]. Either five-iteration SIRT or SART (simultaneous algebraic reconstruction technique) was used for IMOD or AreTomo reconstructions, respectively. Segmentation and rendering were then carried out with the 3D reconstructed tomograms using IMOD.

Germination assay

To evaluate the germination efficiency of *C. difficile* WT and Δ*fezB* spores, around 10⁷ spores were resuspended in 1 ml of BHIS medium amended with 1% taurocholate and incubated at 37 °C. Aliquots (100 μl) of bacterial cultures were collected by centrifugation at different time-points as indicated, resuspended in 100 μl of H_2O and heated at 65 °C for 15 min to remove all vegetative cells. The remaining spores were enumerated on supplemented brain–heart infusion agar (BHISA) plates supplemented with 0.1% taurocholate. The gemination efficiency was monitored for 60 min. Experiments were conducted twice with four biological replicates each time. Data presented are averages of eight replicates (mean ± s.e.m.).

Animal models

All animal experiments under protocol M2000027 were reviewed and approved by the Institutional Animal Care and Use Committee of Vanderbilt University. Procedures were performed according to the institutional policies, Animal Welfare Act, Institutes of Health guidelines and American Veterinary Medical Association guidelines on euthanasia. C57BL/6 male mice (6–8 weeks old; Jackson Laboratories) or *S100a9−/−* mice (6–8 weeks old; bred in-house) were housed in groups of five and maintained at Vanderbilt University Medical Center Animal Facilities.

For the cefoperazone mouse model of CDI, mice were treated with 0.5 mg ml−1 cefoperazone in their drinking water for 5 days, followed by 2 days of recovery with normal drinking water. Mice were then infected via oral gavage with 10⁵ spores in 100 μl of PBS. Before infection, mice were confirmed to be *C. difficile* negative via plating. Body weight and bacterial burden were monitored for 4 days for C57BL/6 mice (Fig. 5a and Extended Data Fig. 10b) and 2 days for *S100a9−/−* mice (Fig. 5o and Extended Data Fig. 10m). For the DSS-induced inflammation mouse model of CDI (Fig. 5d–h and Extended Data Fig. 10e–l), C57BL/6 mice were treated with both 0.5 mg ml−1 cefoperazone and 2.5% DSS in their drinking water for 5 days, followed by 2 days of recovery with normal drinking water. Mice were then infected via oral gavage with 10⁵ spores in 100 μl of PBS. Body weight and bacterial burden were monitored for 2 days. *C. difficile* CFUs were quantified daily from either faecal or caecal samples as indicated, which were homogenized in PBS, serially diluted and plated onto taurocholate cycloserine cefoxitin fructose agar plates for enumeration.

MALDI-IMS

Tissue samples embedded in 2.6% carboxymethylcellulose were cryosectioned at a thickness of 10 μm and mounted onto indium tin oxide-coated glass slides. Tissue sections were washed to remove salts and lipids using a series of 70% ethanol, 100% ethanol, Carnoy's fluid (6 parts ethanol, 3 parts chloroform, 1 part acetic acid), 100% ethanol, 40% ethanol, 100% ethanol. Matrix was then applied to sections using an HTX M5 TM-sprayer containing 3 mg ml−1 (E)-4-(2,5-dihydroxyphenyl) but-3-en-2-one (2,5-cDHA) in 50% ethyl acetate and 50% toluene followed by 9 mg ml−1 2,5-cDHA in 30% ACN, 70% HPLPC-grade water, 0.01% trifluoroacetic acid and 0.005% ammonium hydroxide. The former solution was applied using a 50 °C nozzle temperature, 600 mm min−1 nozzle velocity, 1.5 mm track spacing, 0.05 ml min−1 flow rate and 4 passes, and the latter using 70 °C nozzle temperature, 1,100 mm min−1 nozzle velocity, 1.5 mm track spacing, 0.05 ml min−1 flow rate and 8 passes[43]. MALDI-IMS was performed using a Bruker rapifleX MALDI tissuetyper, a time-of-flight mass spectrometer. The system was operated in linear acquisition mode with 100% laser power, 10 μm laser spot size with beam scan activated (10 μm raster width), 100 laser shots per pixel and approximately 400,000 pixels per tissue section. Data were visualized using SCiLS Lab using root mean square normalization.

Stool specimen collection from paediatric patients

Paediatric participants, aged 12 months to 18 years, were prospectively enroled from July 2017 to December 2019 at Monroe Carell Jr. Children's Hospital at Vanderbilt after informed parental consent and patient assent when applicable. This study was approved by the Vanderbilt Institutional Review Board. Stool samples were collected from (1) non-infected children who were without diarrhoea or a change in their stool pattern and confirmed to be negative for *C. difficile* by nucleic-acid amplification-based testing and (2) symptomatic children with diarrhoea (unformed stools) who underwent clinical laboratory testing and tested positive for *C. difficile* by nucleic-acid amplification-based testing. Thorough medical histories were obtained from all participants, including comorbidities, past hospitalizations, surgeries and medications received 30 days before enrolment, and confirmed by medical record review.

Histopathology and scoring

Intestine samples were prepared as Swiss rolls, fixed in 10% neutral buffered formalin for 48–72 h, routinely processed, embedded in paraffin, sectioned at 5 μm and stained with H&E. H&E-stained slides were evaluated by a veterinary pathologist (K.N.G.-C.) blinded to the composition of the groups. Slides were semiquantitatively scored for the following findings: submucosa oedema, neutrophilic inflammation, enterocyte necrosis/sloughing and mucosal erosion/ulceration on a scale from 0–4, in which: 0 = not present/within normal limits; 2 = mild, rare, scattered; 3 = moderate, multifocal; 4 = marked, locally extensive; 5 = marked, severe, diffuse. The entire slide was evaluated, and the score assigned marked the most severe lesion present as lesions tended to often be multifocal to segmental in nature.

Reporting summary

Further information on research design is available in the Nature Portfolio Reporting Summary linked to this article.

Data availability

All relevant data are within the manuscript and its Supplementary Information. Source data are provided with this paper.

39. Välikangas, T., Suomi, T. & Elo, L. L. A systematic evaluation of normalization methods in quantitative label-free proteomics. *Brief. Bioinform.* **19**, 1–11 (2018).
40. Wagner, F. R. et al. Preparing samples from whole cells using focused-ion-beam milling for cryo-electron tomography. *Nat. Protoc.* **15**, 2041–2070 (2020).

Article

41. Kremer, J. R., Mastronarde, D. N. & McIntosh, J. R. Computer visualization of three-dimensional image data using IMOD. *J. Struct. Biol.* **116**, 71–76 (1996).
42. Zheng, S. et al. AreTomo: an integrated software package for automated marker-free, motion-corrected cryo-electron tomographic alignment and reconstruction. *J. Struct. Biol. X* **6**, 100068 (2022).
43. Yang, J., Norris, J. L. & Caprioli, R. Novel vacuum stable ketone-based matrices for high spatial resolution MALDI imaging mass spectrometry. *J. Mass Spectrom.* **53**, 1005–1012 (2018).

Author contributions H.P. and E.P.S. conceived and designed the experiments. R.S. and Q.Z. performed the cryo-EM, cryo-ET and cryo-FIB-SEM experiments. J.R.M. performed the electron tomography and cryo-FIB-SEM experiments. A.R.S.K. and J.M.S. performed the IMS experiments. K.N.G.-C. performed the histopathology analysis. E.S.K. prepared the bacterial sections using freeze-substitution. M.R.N. collected the human stool samples and clinical isolates. H.P. performed all other experiments. H.P. and E.P.S. wrote the paper with input from all authors. All authors reviewed the paper.

**Competing interests** The authors declare no competing interests.

Additional information
Supplementary information The online version contains supplementary material available at https://doi.org/10.1038/s41586-023-06719-9.
Correspondence and requests for materials should be addressed to Qiangjun Zhou or Eric P. Skaar.
**Peer review information** *Nature* thanks Robert Britton and the other, anonymous, reviewer(s) for their contribution to the peer review of this work. Peer reviewer reports are available.
Reprints and permissions information is available at http://www.nature.com/reprints.
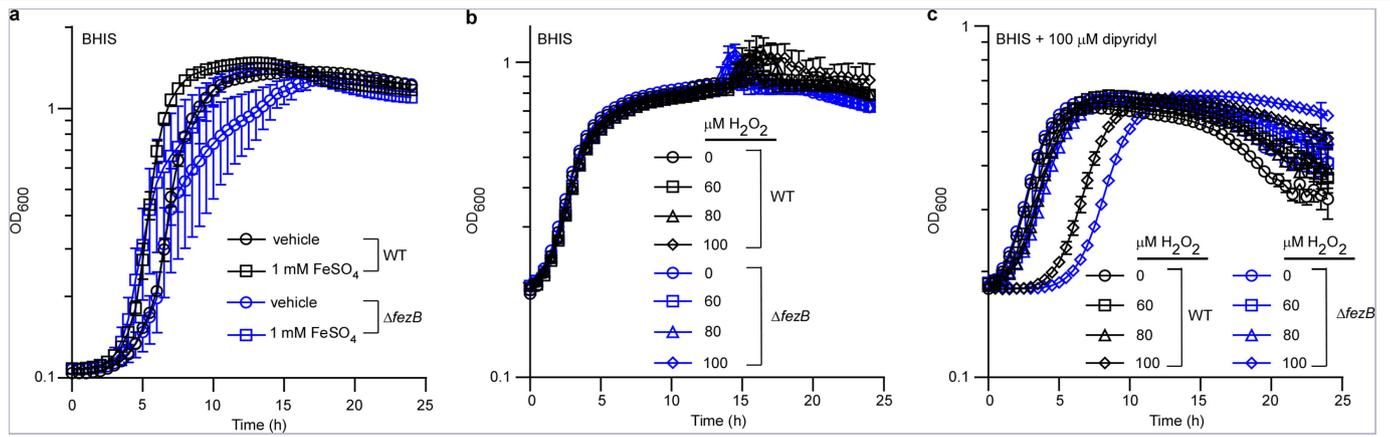
Extended Data Fig. 1 | FezB plays a moderate role in protection against oxidative stress. (**a**) The growth kinetics of *C. difficile* WT and Δ*fezB* grown in BHIS with or without treatment of 1 mM FeSO$_4$. (**b**) Cells were sub-cultured in BHIS and inoculated in BHIS amended with varied concentrations of H$_2$O$_2$. (**c**) Cells were sub-cultured in BHIS supplemented with 100 μM dipyridyl and inoculated in BHIS amended with 100 μM dipyridyl plus varied concentrations of H$_2$O$_2$. Experiments were conducted three times independently with similar results. Data are presented as mean ± STD (n = 3).
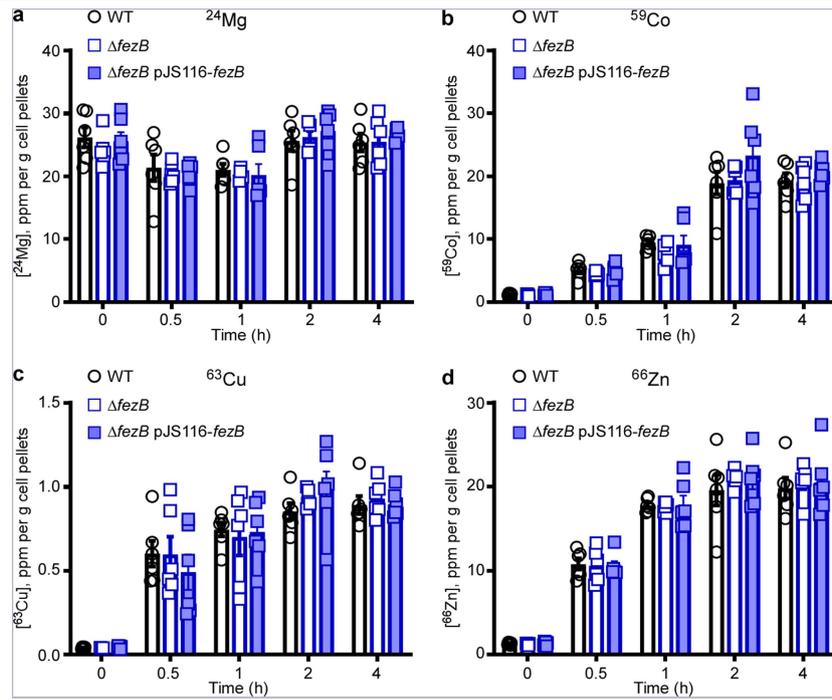
**Extended Data Fig. 2 | Intracellular metal quantification using ICP-MS.** (**a**) The intracellular concentrations of Mg, (**b**) Co, (**c**) Cu, and (**d**) Zn were monitored using ICP-MS for four hours after 1 mM FeSO₄ was added to cultures of *C. difficile* WT, Δ*fezB*, and Δ*fezB* pJS116-*fezB* cells grown in BHIS amended with 100 μM dipyridyl. The data are expressed as parts per million (ppm) per gram cell pellet. Experiments were conducted two times independently with similar results. Data are presented as mean ± SEM (n = 6). No significant differences were observed between strains at each timepoint based on two-tailed t tests.
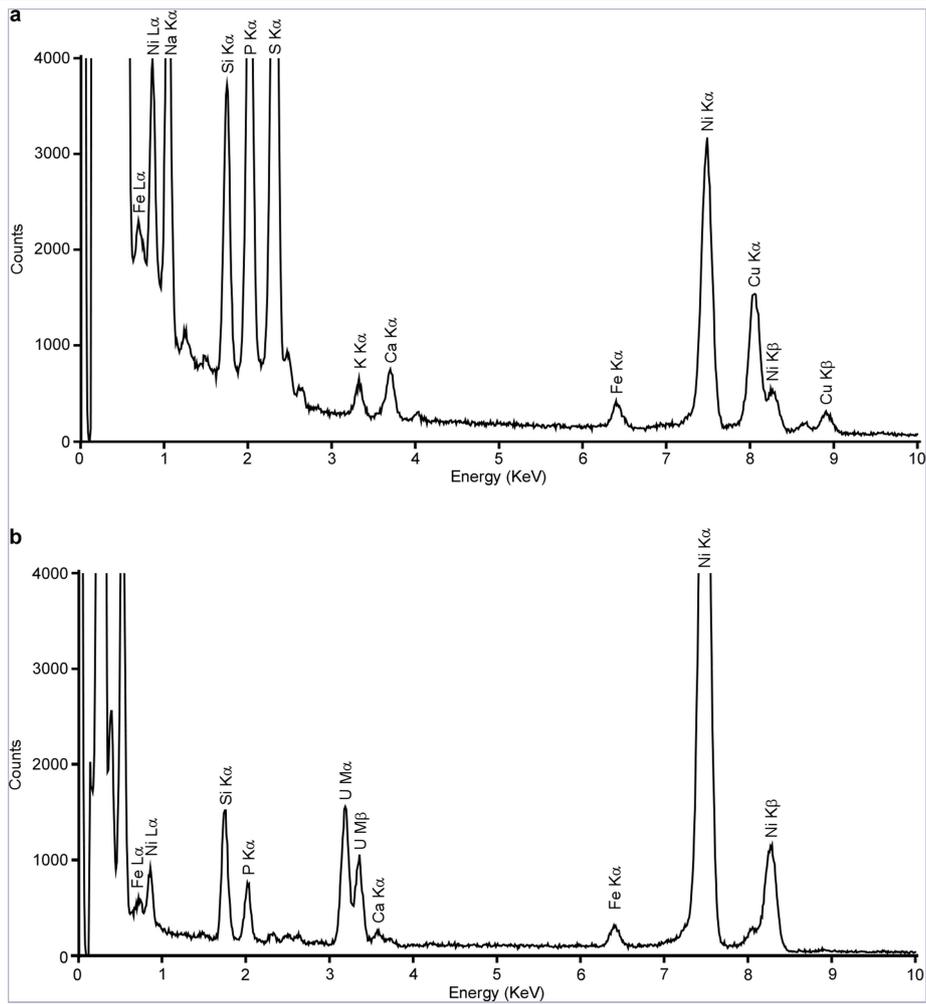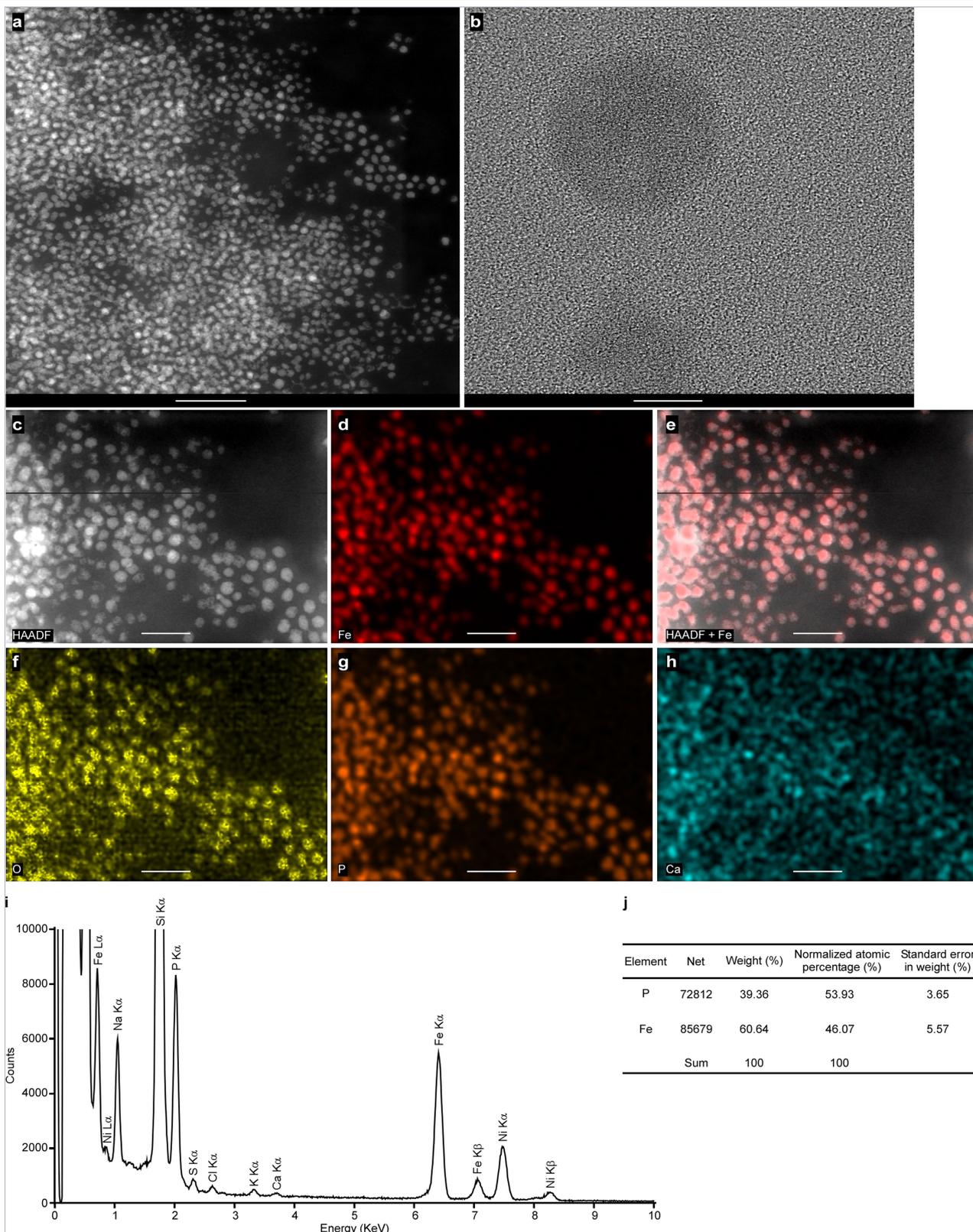
Extended Data Fig. 3 | *C. difficile* produces iron phosphate granules. (a) EDS spectrum of a *C. difficile fur*::CT cell shown in Fig. 3a. The Cu signal was from the tomography holder. (**b**) EDS spectrum of the bacterial section shown in Fig. 3j. The *fur*::CT cells were stained with uranyl acetate and two distinct uranium (U) peaks were observed. Both bacterial cells and sections were deposited on 200 mesh Ni TEM grids, and strong Ni peaks were observed for both sets of samples. Two distinct Fe peaks (Lα and Kα) were evident for both sets but no other transitional metals were detected above background levels.
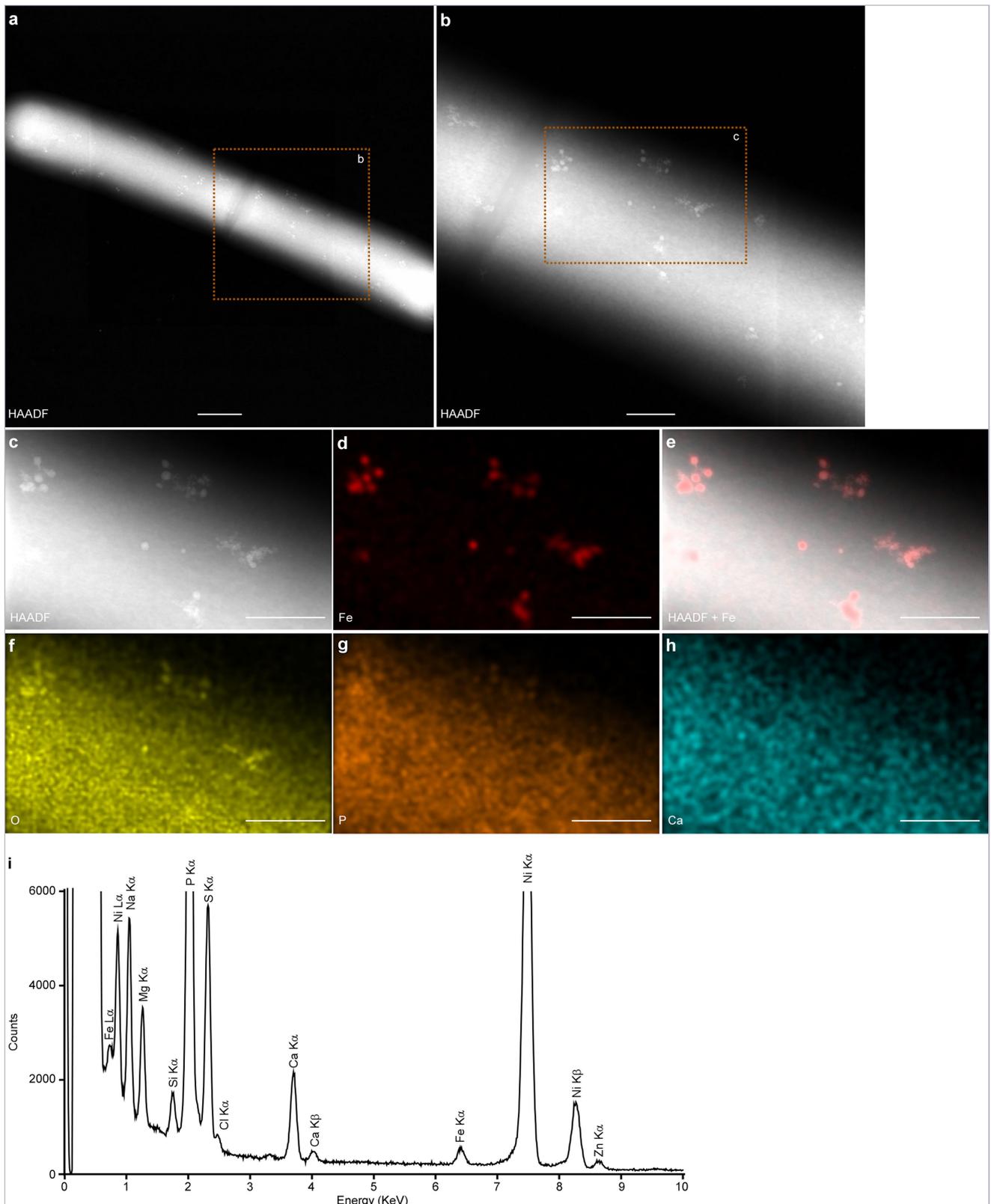
Extended Data Fig. 4 | Clinical isolates produce ferrosomes. (**a**-**b**) Micrographs of *C. difficile* isolate 14 grown in BHIS amended with 150 µM EDDHA for 4 h, followed by addition of 500 µM FeSO$_4$ and 3 h incubation. (**c**-**h**) Representative micrographs of the same cell in panel **b** by (**c**) HAADF-STEM or (**d**-**h**) EDS maps of (**d**) Fe, (**e**) HAADF merged with Fe signal, (**f**) O, (**g**) P, and (**h**) Ca. Scales bars, (**a**) 500 nm and (**b**-**h**) 200 nm. (**i**) The integrated EDS spectrum of the micrograph in panel **c**. Two distinct Fe peaks (Lα and Kα) were detected but no other transitional metals were detected above background levels. The bacterial cells were deposited on 200 mesh Ni TEM grids, and strong Ni peaks were detected. Experiments were conducted using all 12 isolates listed in Table S1 with similar results.

Element	Net	Weight (%)	Normalized atomic percentage (%)	Standard error in weight (%)
P	72812	39.36	53.93	3.65
Fe	85679	60.64	46.07	5.57
Sum		100	100	

Extended Data Fig. 5 | Isolated ferrosomes are amorphous iron- and phosphorus-rich granules. Images shown are (**a**) HAADF-STEM, (**b**) TEM, no crystalline structures were observed in the isolated ferrosomes, (**c**) HAADF-STEM, (**d**) Fe EDS map, (**e**) HAADF merged with Fe signal to show colocalization of Fe signal with electron-dense granules, and EDS maps for (**f**) O, (**g**) P, and (**h**) Ca. (**i**) The integrated EDS spectrum of the isolated ferrosomes shown in panel **c**. Three distinct Fe peaks (Lα, Kα, and Kβ) were observed but no other transitional metals were detected above background levels. Some background signal of Ca was detected. The samples were deposited on 200 mesh Ni TEM grids and strong Ni peaks were detected. Scales bars, (**a**) 200 nm, (**b**) 10 nm, and (**c-h**) 100 nm. (**j**) Elemental quantification based on the EDS spectrum of the isolated ferrosomes. The ratio of P versus Fe is 54:46. Experiments were conducted at least five times with similar results.
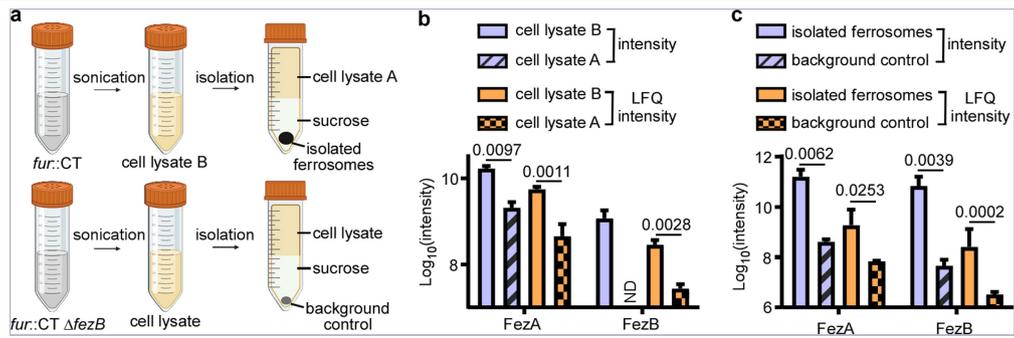
Extended Data Fig. 6 | Identification of ferrosome-associated proteins using liquid chromatography mass spectrometry (LC-MS). (**a**) Schematic of the proteomics experiment. Two comparisons were performed: (**b**) between the cell lysates of *fur*::CT before (cell lysate B) and after ferrosome isolation (cell lysate A), and (**c**) between the isolated ferrosomes from *fur*::CT cells and the background control (*fur*::CT Δ*fezB*). Data shown are both raw intensity and label-free quantification (LFQ) intensity. ND, not detectable. Data are presented as mean ± STD (n = 3). Statistical analyses were done using two-tailed t-test and the p values are denoted in the graphs.
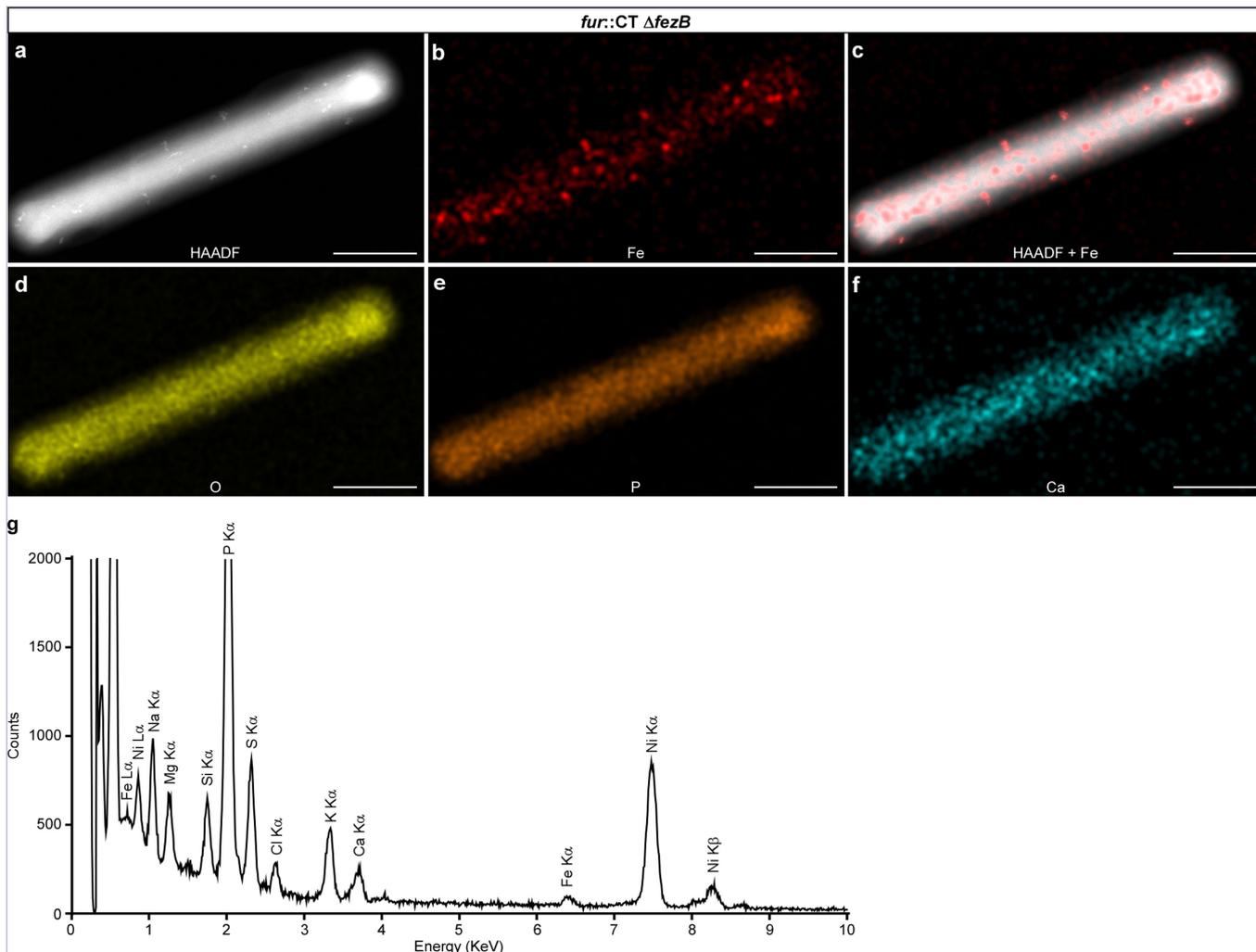
**Extended Data Fig. 7 | Essentiality of FezB in ferrosome formation.**
(**a-f**) Representative micrographs of a *C. difficile fur*::CT Δ*fezB* cell by (**a**) HAADF-STEM or (**b-f**) EDS maps of (**b**) Fe, (**c**) HAADF merged with Fe signal, (**d**) O, (**e**) P, and (**f**) Ca. (**g**) The integrated EDS spectrum of the *fur*::CT Δ*fezB* cell in panel **a**. The bacterial cells were deposited on 200 mesh Ni TEM grids, and strong Ni peaks were observed. Two distinct Fe peaks (Lα and Kα) were detected but only disordered Fe precipitates were observed in this double mutant. No other transitional metals were detected above background levels. Scales bars, 1 μm. Experiments were conducted at least six times with similar results.
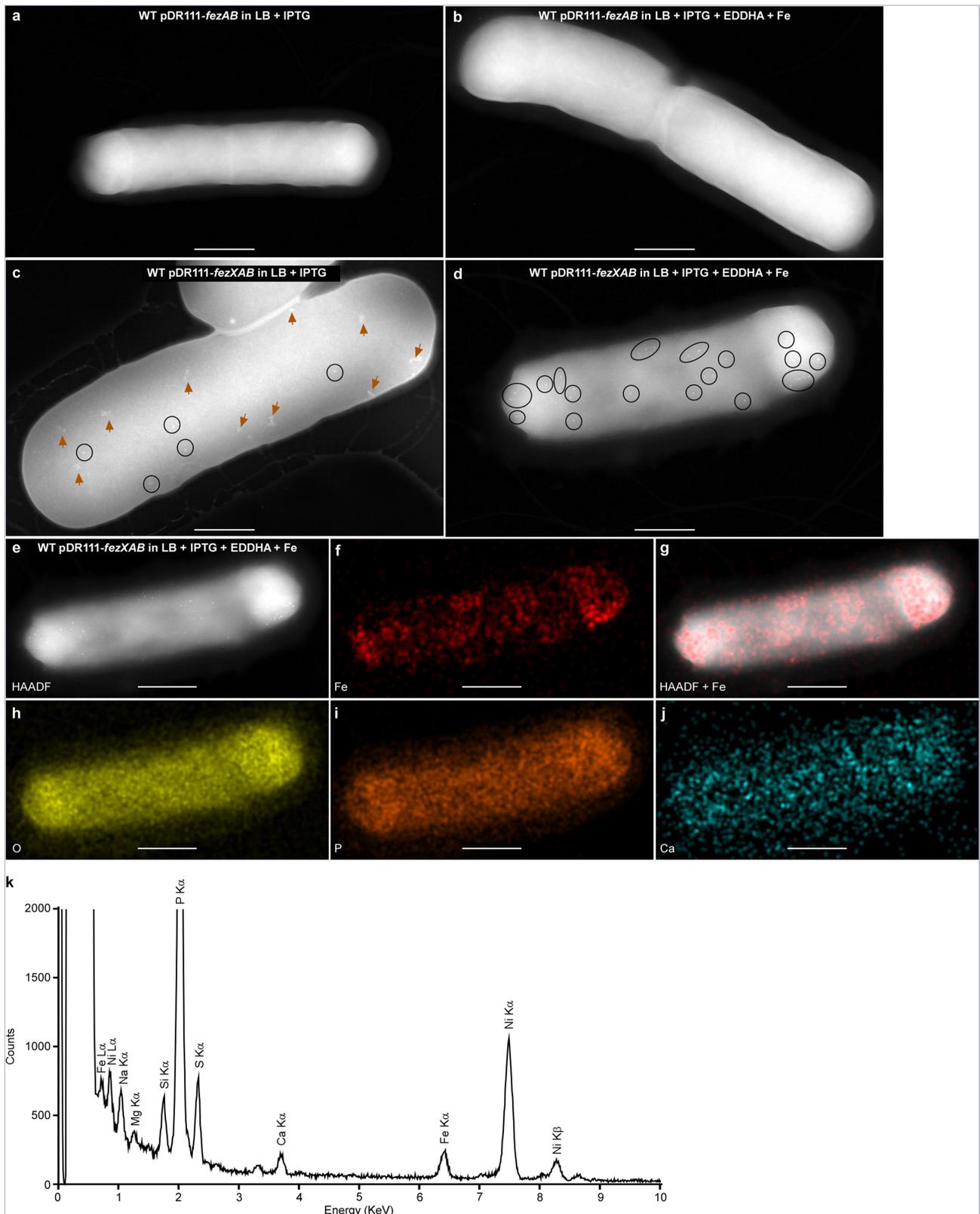
Extended Data Fig. 8 | The entire *fez* operon is required for ferrosome formation in *B. subtilis* 168. (**a-b**) Micrographs of *B. subtilis* cells expressing *fezAB* (WT pDR111-*fezAB*). No electron-dense ferrosomes were observed. (**c-d**) Micrographs of *B. subtilis* cells expressing the entire *fez* operon (WT pDR111-*fezXAB*). Electron-dense granules are circled, and disordered iron precipitates are denoted by orange arrows. (**a** and **c**) Cells were grown anaerobically in LB; (**b** and **d**) Cells were grown anaerobically in LB amended with 100 μM of the iron chelator EDDHA for 4 h, followed by addition of 500 μM FeSO$_4$ and 3 h incubation.

IPTG (1 mM) was used to induce expression of either *fezAB* or the *fez* operon. (**e-j**) Representative micrographs of the same cell in panel **d** by (**e**) HAADF-STEM or (**f-j**) EDS maps of (**f**) Fe, (**g**) HAADF merged with Fe signal, (**h**) O, (**i**) P, and (**j**) Ca. Scale bars, (**a-d**) 500 nm and (**e-j**) 400 nm. (**k**) The integrated EDS spectrum of the micrograph in panel **e**. Two distinct Fe peaks (Lα and Kα) were detected but no other transitional metals were detected above background levels. The bacterial cells were deposited on 200 mesh Ni TEM grids, and strong Ni peaks were detected. Experiments were conducted at least three times with similar results.
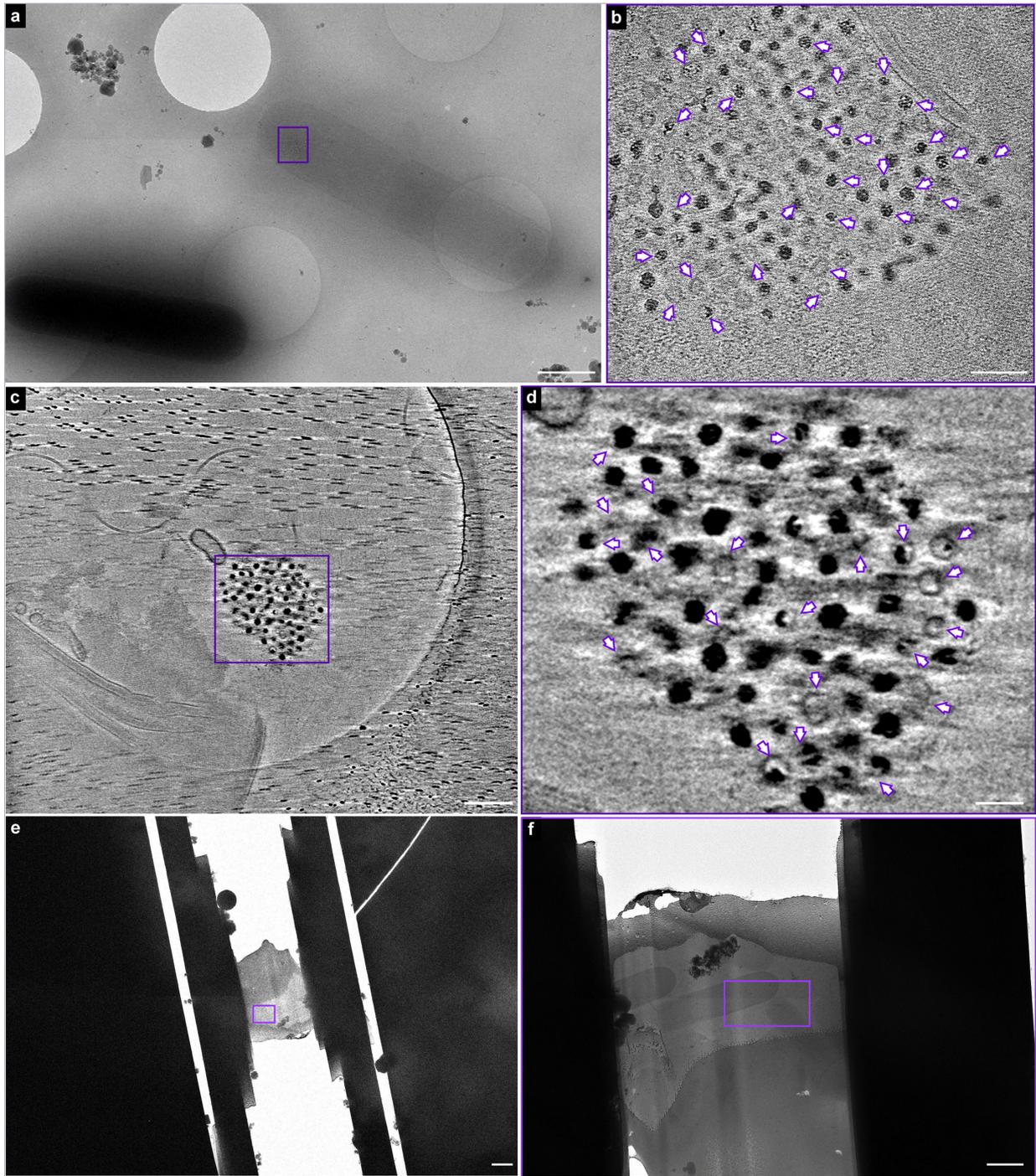
Extended Data Fig. 9 | Cryo-ET reveals that ferrosomes are bound by lipid-like membranes. (**a**) A representative micrograph of *fur*::CT cells visualized using cryo-EM. The cells were processed through rapid vitrification by plunge freezing as described in Methods. A ferrosome cluster evidently present in a thin *fur*::CT cell was selected for cryo-ET (indicated by purple rectangle). (**b**) Cryo-ET reveals lipid-like membrane structures within the ferrosome cluster. The full video of the reconstructed electron tomogram is in Supplemental Video 4. (**c**) A ferrosome cluster was released from lysed *fur*::CT cells during the vitrification process and selected for cryo-ET for better visualization of the ferrosome membrane structures. (**d**) Cryo-ET reveals that membrane vesicles are either empty or filled with varied levels of iron phosphate granules. The full video of the reconstructed electron tomogram is in Supplemental Video 5. The membrane vesicles are annotated by purple arrows. (**e**) A low magnification cryo-EM image shows a FIB-milled lamella containing *fur::CT* cells. (**f**) Zoom-in view of the boxed area as indicated by purple rectangle in panel **e**. The boxed area in panel **f** was selected for cryo-ET and the reconstructed tomogram is shown in Fig. 4h and Supplemental Video 8. Scale bars, (**a**, **f**) 1 μm, (**b**) 100 nm, (**c**) 200 nm, (**d**) 50 nm, and (**e**) 2 μm. Experiments were conducted at least five times with similar results.
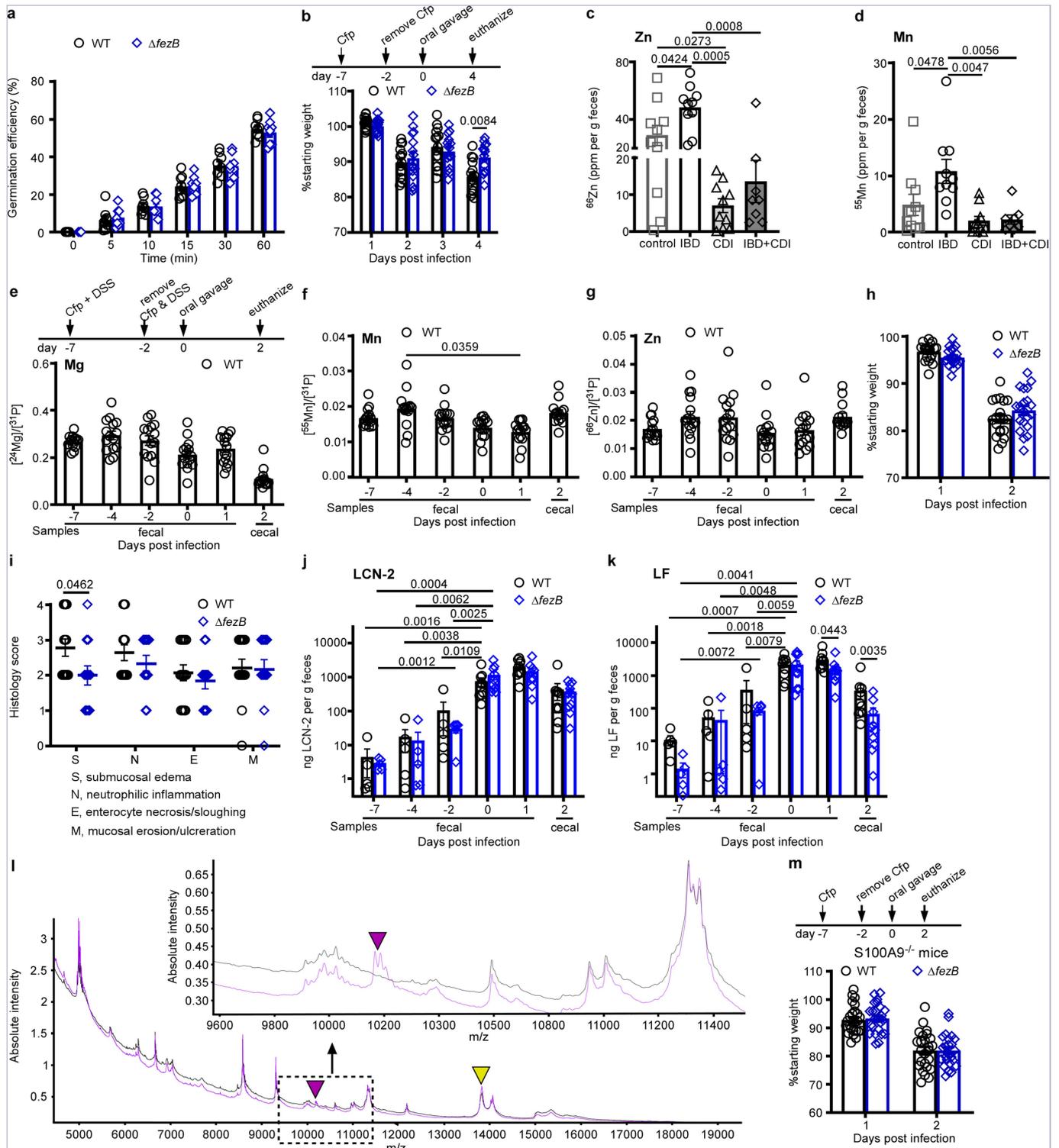
Extended Data Fig. 10 | See next page for caption.

Extended Data Fig. 10 | *C. difficile* resists host-mediated iron sequestration through ferrosome formation. (**a**) Germination efficiency was examined using *C. difficile* WT or Δ*fezB* spores (n = 8). (**b**) Body weight of C57BL/6 J mice infected with *C. difficile* WT or Δ*fezB* spores (n = 20). Mice were treated with cefoperazone (Cfp) prior to infection. (**c**) Zn and (**d**) Mn levels were quantified by ICP-MS in fecal samples from four groups of pediatric patients: control (cancer patients), IBD, CDI, and IBD + CDI. The data are expressed as ppm (parts per million) per gram feces, n = 10 for all groups except the group of IBD + CDI (n = 8). (**e-k**) Infection studies were conducted using an inflammation model where mice were treated with both Cfp and DSS (dextran sulfate sodium) for 5 days (n = 20). (**e**) Mg, (**f**) Mn, (**g**) Zn levels (n = 10), and (**h**) body weight (n = 20) were monitored. (**i**) Histology scores were based on the areas of colon that were most severely affected as pathology was often multifocal to segmental. The scoring rubrics are: 0, not present; 1, mild, rare, scattered; 2, moderate, multifocal; 3, marked, locally extensive; and 4, marked, severe, diffuse. (**j**) Lipocalin (LCN−2) and (**k**) lactoferrin (LF) levels were quantified during infection. (**l**) MALDI IMS spectrum showing protein signals, including those associated with calprotectin (S100A8, *m/z* 10,164, indicated by a purple triangle) and an unidentified protein (*m/z* 13,807, annotated by a yellow triangle) from murine colon tissue from S100A9$^{-/-}$ (black) or C57BL/6 J (purple) mice infected with *C. difficile* WT spores. (Inset) Selected window from the protein MALDI IMS spectrum showing protein signal from calprotectin (S100A8, *m/z* 10,164 indicated with a purple arrow). (**m**) Body weight of S100A9$^{-/-}$ mice infected with *C. difficile* WT or Δ*fezB* spores (n = 25). Mice were treated with Cfp prior to infection. (**e-g**, **j-k**, and **m**) Fecal samples were used for all timepoints except the end timepoint (day 2 or 4), when the mice were euthanized and cecal samples were used. All data are mean ± SEM. Statistical analyses were done using (**a-b**, **h-i**, **m**) two-tailed t tests, (**j-k**) two-way ANOVA, or (**c-g**) one-way ANOVA and the significant p values are denoted in the graphs.

nature portfolio

Corresponding author(s): Eric P Skaar

Last updated by author(s): Sep 11, 2023

Reporting Summary

Nature Portfolio wishes to improve the reproducibility of the work that we publish. This form provides structure for consistency and transparency in reporting. For further information on Nature Portfolio policies, see our Editorial Policies and the Editorial Policy Checklist.

Statistics

For all statistical analyses, confirm that the following items are present in the figure legend, table legend, main text, or Methods section.

n/a	Confirmed	
☐	☒	The exact sample size (*n*) for each experimental group/condition, given as a discrete number and unit of measurement
☐	☒	A statement on whether measurements were taken from distinct samples or whether the same sample was measured repeatedly
☐	☒	The statistical test(s) used AND whether they are one- or two-sided *Only common tests should be described solely by name; describe more complex techniques in the Methods section.*
☒	☐	A description of all covariates tested
☐	☒	A description of any assumptions or corrections, such as tests of normality and adjustment for multiple comparisons
☐	☒	A full description of the statistical parameters including central tendency (e.g. means) or other basic estimates (e.g. regression coefficient) AND variation (e.g. standard deviation) or associated estimates of uncertainty (e.g. confidence intervals)
☐	☒	For null hypothesis testing, the test statistic (e.g. *F*, *t*, *r*) with confidence intervals, effect sizes, degrees of freedom and *P* value noted *Give P values as exact values whenever suitable.*
☒	☐	For Bayesian analysis, information on the choice of priors and Markov chain Monte Carlo settings
☒	☐	For hierarchical and complex designs, identification of the appropriate level for tests and full reporting of outcomes
☒	☐	Estimates of effect sizes (e.g. Cohen's *d*, Pearson's *r*), indicating how they were calculated

Our web collection on statistics for biologists contains articles on many of the points above.

Software and code

Policy information about availability of computer code

Data collection	We did not generate any custom software or algorithm for this study. We used the following software program for cryoET data collection: Thermo Fisher Tomography (version 5.14).
Data analysis	We did not generate any custom software or algorithm for this study. We used the following software programs for cryoET data analysis: cryoET reconstruction: AreTomo (version 1.1.1) and cryoET Reconstruction and segmentation: IMOD (version 4.11.15).

For manuscripts utilizing custom algorithms or software that are central to the research but not yet described in published literature, software must be made available to editors and reviewers. We strongly encourage code deposition in a community repository (e.g. GitHub). See the Nature Portfolio guidelines for submitting code & software for further information.

Data

Policy information about [availability of data](#)

All manuscripts must include a [data availability statement](#). This statement should provide the following information, where applicable:
- Accession codes, unique identifiers, or web links for publicly available datasets
- A description of any restrictions on data availability
- For clinical datasets or third party data, please ensure that the statement adheres to our [policy](#)

> All relevant data are within the manuscript and its Supplementary Information. We have included a Data Availability Statement in the manuscript.

Human research participants

Policy information about [studies involving human research participants and Sex and Gender in Research.](#)

Reporting on sex and gender	The information of sex and gender was collected and considered during patient recruitment. However, sex or gender-based analysis was not performed due to limited size of the patient pools.
Population characteristics	Median age of the human research participants was 11 years (IQR 7-14) 22 (58%) were female 2 (5%) Hispanic 32 (84%) White 6 (16%) Black
Recruitment	Recruitment: Pediatric participants, ages 12 months through 18 years, with a diagnosis of C. difficile infection or a comorbidity of interest (cancer, inflammatory bowel disease) who received care at Monroe Carell Jr. Children's Hospital at Vanderbilt were eligible for enrollment. To minimize self-selection bias, all eligible patients were contacted by study personnel via phone call or in person at the time of a clinical encounter. Stool samples were collected from (1) non-infected children who were without diarrhea or a change in their stool pattern, and confirmed to be negative for C. difficile by nucleic-acid amplification-based testing (NAAT) and (2) symptomatic children with diarrhea (unformed stools) who underwent clinical laboratory testing and tested positive for C. difficile by NAAT. Thorough medical histories were obtained from all participants, including comorbidities, past hospitalizations, surgeries, and medications received 30 days prior to enrollment and confirmed by medical record review.
Ethics oversight	This study was approved by the Vanderbilt Institutional Review Board.

Note that full information on the approval of the study protocol must also be provided in the manuscript.

Field-specific reporting

Please select the one below that is the best fit for your research. If you are not sure, read the appropriate sections before making your selection.

☒ Life sciences ☐ Behavioural & social sciences ☐ Ecological, evolutionary & environmental sciences

For a reference copy of the document with all sections, see [nature.com/documents/nr-reporting-summary-flat.pdf](#)

Life sciences study design

All studies must disclose on these points even when the disclosure is negative.

Sample size	No statistical method was used to predetermine sample size. We carefully determined the sample size for each experiment to ensure that the data possesses adequate statistical power for detecting significant differences between the groups. Our primary objective in designing the sample sizes was to strike a balance between minimizing errors, whether false positives or false negatives, while also avoiding the unnecessary inflation of experiment sizes. This approach helps us mitigate potential issues related to cost, logistical challenges, and ethical considerations. In addition, we repeated each experiment independently multiple times to ensure reproducibility.
Data exclusions	No data were excluded from analysis.
Replication	All experiments were performed independently at least three times. Due to the nature of science experimentation, not all attempts were successful. But we were able to repeat each experiment successfully at least three times.
Randomization	Experimental groups were formed according to genotype, where necessary, or randomized, where possible.
Blinding	This study did not involve any experimental subject group; therefore, experimenter binding did not apply and was not performed.

Reporting for specific materials, systems and methods

We require information from authors about some types of materials, experimental systems and methods used in many studies. Here, indicate whether each material, system or method listed is relevant to your study. If you are not sure if a list item applies to your research, read the appropriate section before selecting a response.

Materials & experimental systems

n/a	Involved in the study
☒	☐ Antibodies
☒	☐ Eukaryotic cell lines
☒	☐ Palaeontology and archaeology
☐	☒ Animals and other organisms
☒	☐ Clinical data
☒	☐ Dual use research of concern

Methods

n/a	Involved in the study
☒	☐ ChIP-seq
☒	☐ Flow cytometry
☒	☐ MRI-based neuroimaging

Animals and other research organisms

Policy information about studies involving animals; ARRIVE guidelines recommended for reporting animal research, and Sex and Gender in Research

Laboratory animals	C57BL/6 male mice (6–8 week old; Jackson Laboratories) and S100A9–/– (6–8 week old; bred in-house) were used in this study. Mice were housed at Vanderbilt University Medical Center Animal facility with temperature between 69-75 degree Fahrenheit and humidity between 30-70%. A 12-hour light-dark cycle were maintained. Mice were housed in groups of five with free access to autoclaved water and food. All experimental manipulations were performed in a biosafety level 2 laminar flow hood.
Wild animals	No wild animals were used in this study.
Reporting on sex	C57BL/6 male mice (6–8 week old; Jackson Laboratories) were used. S100A9–/– (6–8 week old; bred in-house), both female and male mice were used in this study. Sex or gender-based analysis was not conducted because only male C57BL/6 mice were used.
Field-collected samples	No field collected samples were used in this study.
Ethics oversight	All animal experiments under protocol M2000027 were reviewed and approved by the Institutional Animal Care and Use Committee of Vanderbilt University.

Note that full information on the approval of the study protocol must also be provided in the manuscript.